Journal of Pharmaceutical Innovation (2026) 21:80
https://doi.org/10.1007/s12247-025-10245-8

RESEARCH

Combination Therapy Using Bilosome–Chitosan Nanocarriers for Effective Drug Delivery of Daclatasvir and Xanthone in COVID-19 and Acute Respiratory Distress Syndrome: A Preclinical Assessment

Marwa H. S. Dawoud[1] · Heba T. Elbalkiny[1] · Amr Abdelhamid[1] · Mai A. Amer[1] · Reham Wasfi[1] · Mai A. Zaafan[1]

Received: 31 May 2025 / Accepted: 1 November 2025

Abstract

Purpose COVID-19 pandemic has driven the urgent need for effective antiviral treatments and strategies to combat its life-threatening complications. This study aims to develop a combination therapy approach using daclatasvir, as an antiviral agent, and xanthone, as a potent anti-inflammatory and antithrombotic compound, delivered via Bilosome-Chitosan Nanoparticles (BCNP).

Methods The impact of varying the bilosome-to-chitosan ratio on the particle size (PS), zeta potential (ZP), and encapsulation efficiency (EE%) was evaluated. An optimized formula was prepared and tested for its antiviral activity and its potential for pulmonary protection in acute respiratory distress syndrome (ARDS) on mice model.

Results The optimized formulation (O_1) showed a PS of 222.67 nm, a polydispersity index of 0.368, a ZP of -19.10 mV, and EE% of 83.78% for xanthone and 78.98% for daclatasvir. Controlled release profiles were attained, with daclatasvir released over 24 h and xanthone sustained for up to 72 h. The optimized formula showed promising deposition lung profile when tested using MPPD modelling. O_1 demonstrated strong antiviral activity against SARS-CoV-2, with a selectivity index (SI = 5.02) and an IC50 of 3.87 μM. Additionally, the formulation exhibited pulmonary protective effects by modulating the LncGAS5/ACE2 pathway, with significant improvements in the lungs of the mice model, offering a potential therapeutic strategy against ARDS, a severe and often fatal COVID-19 complication.

Conclusion A successful BCNP formulation combining daclatasvir and xanthone was prepared, providing a promising combination therapy approach for COVID-19 treatment and ARDS prevention.

Keywords Xanthenone · Daclatasvir dihydrochloride · Optimization · Acute respiratory distress syndrome · SARS-CoV-2

✉ Marwa H. S. Dawoud
mdawoud@msa.edu.eg

Heba T. Elbalkiny
htarek@msa.edu.eg

Amr Abdelhamid
aabdelhamid@msa.edu.eg

Mai A. Amer
mwahed@msa.edu.eg

Reham Wasfi
rwasfi@msa.edu.eg

Mai A. Zaafan
makamel@msa.edu.eg

[1] October University of Modern Sciences and Arts, Cairo, Egypt

Abbreviations

ACE	Angiotensin Converting Enzyme
AD	AeroDynamic Diameter
ARDS	Acute Respiratory Distress Syndrome
BCNP	Bilosome-Chitosan Nanoparticles
CC50	Half-Maximal Cytotoxic Concentration
COX	Cyclooxygenase
CS-NPs	Chitosan Nanoparticles
DAB	DiAminoBenzidine
DL%	Drug Loading Percentage
DLS	Diffractive Light Scattering
DMEM	Dulbecco's Modified Eagle Medium
DMSO	Dimethyl Sulfoxide
EE%	Entrapment Efficiency Percentage
GSD	Geometric Standard Deviation
HCV	Hepatitis C Virus

Published online: 29 December 2025

IC50	Inhibitory Concentration 50
LncGAS5	Long Non-Coding RNA GAS5
LPS	Lipopolysaccharide
MMAD	Mass Median Aerodynamic Diameter
MPPD	Multiple Path Particle Dosimetry
PBS	Phosphate Buffered Saline
PCR	Polymerase Chain Reaction
PS	Particle Size
PDI	Polydispersity Index
RT	Room Temperature
SARS-CoV-2	Severe Acute Respiratory Syndrome Coronavirus 2
SI	Selectivity Index
SP-1	Pulmonary Surfactant Protein-1
TNF-α	Tumor Necrosis Factor Alpha
ZP	Zeta Potential

Introduction

SARS-CoV-2, (Severe Acute Respiratory Syndrome CoronaVirus 2) the virus responsible for COVID-19, is a member of the beta coronavirus family within the *Sarbecovirus subgenus*, which is a new coronavirus related to both SARS-CoV-2 and Middle East Respiratory Syndrome CoronaVirus (MERS-CoV). This virus has prompted the World Health Organization to announce it as pandemic in 2020, due to its worldwide transmission. It has been reported to cause severe anemia and high fatality rate [1]. It causes acute respiratory distress syndrome (ARDS), and multiple organ failure, leading to severe acute respiratory failure with high mortality rates [2]. ARDS, the major complication of respiratory tract infection is an inflammatory process in the lungs that results in non-hydrostatic protein-rich pulmonary oedema. ARDS leads to immediate effects such as severe hypoxaemia, reduced lung compliance, and increased intrapulmonary shunt and dead space. The clinicopathological features include severe inflammatory damage to the alveolar-capillary barrier, surfactant depletion, and loss of aerated lung tissue [3]. Management of COVID-19 infection and its ARDS complication could be derived from the treatments that have been used during the SARS-CoV or MERS-CoV pandemics or from in-vitro observations [4].

Xanthones are a class of naturally occurring polyphenolic compounds predominantly found in the fruit of *Garcinia mangostana* L. (family: Clusiaceae), commonly known as mangosteen, and have been reported to exhibit diverse biological activities. Among these, 9-xanthenone has demonstrated significant anti-inflammatory properties, notably through the inhibition of cyclooxygenase (COX) enzymes, which are key mediators in the inflammatory cascade. This compound has recently been synthesized chemically, suggesting potential therapeutic applications in maintaining pulmonary health [5] In addition, xanthones appear to provide antioxidant, antithrombotic, and antiviral benefits [6]. Besides that, xanthones have also been highly proven to exhibit immunomodulatory activities [7]. Xanthones have demonstrated the ability to block SARS-CoV-2 entry into host cells by inhibiting ACE2 and Mpro, in addition to that as activators of the ACE2/Angiotensin 1–7 axis, xanthones also offer neuroprotective effects against cerebral ischemia/reperfusion injury through antioxidant, anti-inflammatory, and anti-apoptotic mechanisms [8]. Additionally, they have shown protective effects against myocardial damage in isoprenaline-induced rat models [9] and have been reported to alleviate vascular and pulmonary hypertension, alveolar remodeling, and related conditions [10].

Whereas daclatasvir is an antiviral drug that targets hepatitis C virus (HCV) replication. It works by binding to the front end (N-terminus) of HCV non-structural protein 5 A, or NS5A, which inhibits two key steps in the HCV life cycle; copying its RNA genetic material and assembling new virus particles. NS5A is a protein that has several roles, including assisting viral RNA replication, supporting steps related to HCV infection of cells, and blocking interferon pathways used by the immune system. SARS-CoV-2 has a large genome and encodes 16 non-structural proteins numbered nsp1 to nsp16. These SARS-CoV-2 nsps carry out similar functions to NS5A in HCV, such as viral replication and evasion of host immunity. Accordingly, NS5A with daclatasvir blocks HCV and SARS-CoV-2 replication, which could block SARS-CoV-2 replication as well, leading to the management of the viral replication [11]. The use of daclatasvir for SARS-CoV-2 management had been reported in human respiratory cell lines by targeting viral RdRp and ExoN activities, showing promising results [12].

A good control of COVID-19 could be accomplished through combining daclatasvir (as an antiviral) with xanthone (as an anti-inflammatory and antioxidants) [13], which exhibits many beneficial applications in COVID-19 management. However, xanthone suffers poor bioavailability owing to its poor solubility, which could hinder its potential use [14]. Furthermore, combining both therapeutic agents into a single dosage form is crucial, provided that their full activity is maintained and no interaction occurs between them.

Bilosome-chitosan nanoparticles (BCNP) is a drug delivery system that may enclose more than one drug together for certain applications, and overcome the poor bioavailability of some drugs, with controlled release. Bilosomes are tiny spherical structures consisting of one or more lipid bilayers with bile salts that form spontaneously when phospholipids are hydrated in aqueous solutions [15], which allow lipophilic drugs to be dispersed in aqueous media, making it

suitable for nebulization [16]. Whereas chitosan nanoparticles have garnered much attention lately as polymer-based drug delivery vehicles that can improve biodistribution, specificity, efficacy, and safety profiles as compared to free drugs, which enable non-invasive administration routes such as nasal, oral, ocular, and inhalation without causing any harms being biocompatible and biodegradable. Overall, the multifunctional capabilities of chitosan nanoparticles highlight their potential use for application as customized release systems for a variety of pharmacological agents, with the advantages of targeted therapy and reduced toxicity. The improved absorption and protection afforded by encapsulation into chitosan nanoparticles greatly expands possible therapeutic applications [17]. Furthermore, chitosan has been widely used as anti-inflammatory, antimicrobial and antioxidant effects [18], which could have a direct impact in the prophylaxis against ARDS. Moreover, chitosan-based systems are mucoadhesive, allowing the formulation to adhere to pulmonary mucosa and extend drug retention [19]. In addition to that, encapsulation into nanoparticles can protect the drugs from oxidative or enzymatic degradation in the lung environment [20].

Extensive research has established chitosan nanoparticles as superior carriers for pulmonary drug delivery. Zacaron et al., 2023 comprehensively reviewed chitosan nanoparticles for pulmonary delivery, highlighting their intrinsic biological properties including anti-inflammatory, antimicrobial, and mucoadhesive capacities. However, they noted challenges with particle aggregation and exhalation, which the current bilosome-chitosan approach aims to address [21]. While individual studies have explored xanthone and daclatasvir separately, no previous research has investigated their co-delivery in a single formulation for COVID-19 and ARDS management.

The co-encapsulation of xanthone and daclatasvir within a bilosome–chitosan nanoparticle system presents a promising combinational therapeutic strategy against COVID-19 and its severe complication, ARDS. The combination of these agents in a single nanocarrier enables synergistic pharmacological effects by simultaneously targeting viral replication and the downstream inflammatory cascade.

The current bilosome-chitosan complex represents a novel approach for simultaneous delivery of hydrophobic and hydrophilic drugs. Furthermore, while separate mechanistic studies exist for xanthone (anti-inflammatory) and daclatasvir (antiviral), the current study provides the first comprehensive evaluation of their combined effects through the LncGAS5/ACE2 pathway.

Previous pulmonary delivery systems faced limitations with either rapid clearance (liposomes) or limited drug loading (chitosan alone). The bilosome-chitosan complex addresses both challenges simultaneously.

This study aims to develop a novel combination nanotherapy combining daclatasvir and xanthone within bilosome–chitosan nanoparticles to effectively combat SARS-CoV-2 infection and prevent severe complications like ARDS, in an attempt to achieve synergistic therapeutic effects by simultaneously targeting viral replication and the inflammatory/thrombotic complications of COVID-19, thereby enhancing treatment efficacy and reducing disease severity through a single, co-delivered nanocarrier system.

Experimental

Materials

Xanthone (Xanthen-9-one) ($C_{13}H_8O_2$, CAS No.: 90-47-1, Molecular Weight: 196.20), Cholesterol, 95%, Soduim tripolyphosphate and Chitosan (Medium molecular weight) were purchased from Sigma-Aldrich (MO, USA). Daclatasvir dihydrochloride was supplied as a gift from Marcyrl Pharmaceutical Industries (Cairo, Egypt). Glacial acidic acid was purchased from Piochem (Giza, Egypt), Methylene Chloride was purchased from Diachem Chemicals (Sant'Alessandro, Italy) and Soduim Deoxycholate 90% was procured from Loba Chimie Pvt. Ltd (Mumbai, India). Trehalose dehydrate, methanol and ethanol HPLC grade were purchased from Advent Chemie Pvt. Ltd. (Mumbai, India). Soybean phosphotidyl choline (Lecithin, 90%) was purchased from Alfa Aesar through Thermo Fisher Scientific (Ward Hill, MA, USA). Endotoxin lipopolysaccharide (LPS) from gram-negative bacteria E. coli were purchased from Sigma-Aldrich (St. Louis, MO, USA).

Preparation of Nanoparticles

Preparation of Chitosan Nanoparticles

Chitosan nanoparticles (CS-NPs) were prepared via ionic gelation technique. A 1% (w/v) chitosan solution was first prepared in 1% (v/v) acetic acid, into which 60 mg of daclatasvir dihydrochloride was dissolved directly. For both the drug-loaded and blank formulations, chitosan solution (with or without daclatasvir dihydrochloride, respectively) was added dropwise into an aqueous tripolyphosphate solution (1 mg/mL) under magnetic stirring at 500 rpm (MMS-3000, Biosan LTD, UK) at room temperature. Stirring was maintained for 2 h to facilitate nanoparticle formation. The resulting CS-NPs were then collected by centrifugation at 16,000 ×g (Megafuge 16R, Hanau, Germany) for 30 min, and the nanoparticles were resuspended in deionized water for further characterization and subsequent incorporation into BCNP, as described by Diebold Y, et al., 2006 [22].

Preparation of Bilosomes

Bilosomes were prepared using the thin-film hydration method. A total of 150 mg of a lipid mixture, comprising phosphatidylcholine and cholesterol in a 3:1 molar ratio, was dissolved in methylene chloride, with or without 20 mg of xanthone to form the drug-loaded or the blank formulation, respectively. The organic solvent was then completely evaporated using a rotary evaporator (Heidolph 2, Schwabach, Germany) for 30 min, forming a thin lipid film on the inner wall of the flask. This film was subsequently rehydrated with an aqueous sodium deoxycholate solution (15% w/v), prompting the self-assembly of bilosomal vesicles and encapsulation of xanthone. The resulting dispersion was sonicated for 5 min to ensure uniform vesicle formation, followed by overnight refrigeration to promote vesicle maturation, as described by Sweed NM, et al., 2024 [23].

Preparation of bilosome-chitosan Nanoparticles

BCNP were prepared by mixing bilosome and CS-NPs dispersions together at different ratios (as presented in Table 1), followed by freeze-drying. To stabilize the BCNP during lyophilization, 5.0% trehalose was added as a cryoprotectant prior to freezing and drying. This method allowed integration of chitosan nanoparticles into the lipid bilayers of the bilosomes, and coating of bilosomes to the CS-NPs, yielding dried BCNP, which could be rehydrated for further use. The inclusion of trehalose effectively protected the complex morphology during freeze-drying, ensuring the reconstitution capability of the dried product [22]. The lyophilized nanoparticles formulation was reconstituted in distilled water prior to use for characterization and biological evaluation.

A pilot study was conducted in which chitosan nanoparticles and bilosomes were first prepared separately and characterized. Upon attempting to combine them into a complex, it was observed that bilosome: chitosan ratios below 1:1 and above 3:1 were unsuccessful in producing stable nanoparticle complexes. These unsuccessful formulations failed to achieve acceptable particle size (PS), polydispersity index (PDI), zeta potential (ZP), and encapsulation efficiency (EE%) for either xanthone or daclatasvir. Only ratios within the range of 1:1 to 3:1 allowed for favorable physicochemical properties and proper co-encapsulation of both drugs (Supplementary S-1), thus these were the levels used in the experimental design.

Experimental Design

A one-factor experimental design was employed to evaluate the effect of varying bilosomes: chitosan nanoparticles ratio (w/w) (X_1) across 5 levels, on several response outcomes. The selected ratios were designed to span a practical range from lipid-rich to polymer-rich nanoparticles systems, enabling systematic evaluation of how chitosan content influences particle size, surface charge, and encapsulation efficiency of the co-loaded drugs. Previous studies on liposome–chitosan complexes have frequently employed a 2:1 ratio for optimization [24, 25]; therefore, we extended this range both above (up to 3:1) and below (down to 1:1) in order to investigate the effect of varying complexation levels within limits that support stable nanoparticle formation and optimal drug delivery performance. The measured responses resulting from varying X_1 across the 5 levels were: particle size (PS) (Y_1); zeta potential (ZP) (Y_2); entrapment efficiency percentage of xanthone (EE% of X) (Y_3); and entrapment efficiency percentage of daclatasvir dihydrochloride (EE% of D) (Y_4), are presented in Table 1.

Table 1 Formulation code and composition, and their measured responses, with the responses' constraints

Formula code	Bilosomes: chitosan nanoparticles (X_1)	Particle Size (nm) (Y_1)	Zeta Potential (mV) (Y_2)	Entrapment Efficiency of Xanthone (%) (Y_3)	Entrapment Efficiency of Daclatasvir (%) (Y_4)
F1	2:1	200.0 ± 10.5	-16.1 ± 1.1	78.7 ± 3.8	76.1 ± 3.8
F2	1:1	255.7 ± 15.7	-16.9 ± 1.9	90.0 ± 2.8	66.8 ± 1.5
F3	3:1	229.5 ± 8.8	-13.1 ± 0.4	79.1 ± 3.6	80.4 ± 2.7
F4	2.5:1	279.9 ±16.9	-19.0 ± 2.6	88.2 ± 2.9	71.3 ± 3.2
F5	1.5:1	246.1 ±13.6	-9.6 ± 1.6	88.1 ± 2.8	70.3 ± 4.2
Responses					Constraints
Particle Size (nm) (Y_1)					50-500 nm
Zeta Potential (mV) (Y_2)					Maximize
Entrapment Efficiency of Xanthone % of X (Y_3)					Maximize
Entrapment Efficiency of Daclatasvir (Y_4)					Maximize

Results are presented as mean ± SD

Formulation Optimization

Formulation optimization was carried out to determine the optimal conditions for producing the desired nanoparticle formulation while meeting predefined constraints. Specifically, the target particle size was set between 50 and 500 nm, as studies have shown that nanoparticles smaller than 50 nm are often exhaled before deposition, while those larger than 500 nm tend to accumulate in the upper respiratory tract [21]. Additionally, the goal was to maximize zeta potential to enhance formulation stability, and to achieve the highest possible encapsulation efficiency for both drugs. Optimization was conducted using the Design-Expert 13.0.5.0 software (Stat-Ease Inc. in the USA), adopting numerical optimization based on desirability approach. The optimized formulation suggested by the software (O_1) was subsequently prepared and evaluated by measuring the same response variables mentioned before. The actual experimental results obtained were compared to the predicted results to calculate the % bias [26].

Characterization of BCNP

Measurement of Particle size, Polydispersity Index and Zeta Potential

The PS, polysidpersity index and the ZP of the vesicular nanoparticles were measured by dynamic light scattering method (DLS), using a zetasizer at 25 °C (Malven Zetasizer version 6.20 serial number: MAL 104 4595, Worcestershire, UK), after rehydrating the lyophilized powder with distilled water. Each sample was analyzed in triplicate using at least three independent preparations [27].

Measurement of Entrapment efficiency% and Drug loading%

The entrapment efficiency (EE%) and drug loading (DL%) of BCNP were measured following the centrifugation of the nanoparticle dispersion at 15,300 Xg, using a cooling centrifuge (Megafuge 16R, Hanau, Germany) to separate the free unentrapped drugs in the supernatant from the drug-loaded nanoparticles. The precipitate was washed twice with distilled water to remove the unentrapped drug, and the amount of free drug in the supernatant was measured spectrophotometrically using the first derivative method. The EE% of the drugs and the drug loading% were calculated according to Eqs. 1 and 2, respectively [28].

$$EE\% = \left(1 - \frac{amount\ of\ drug\ in\ the\ supernatant}{amount\ of\ added\ drug}\right) * 100 \quad (1)$$

$$DL\% = \left(1 - \frac{weight\ of\ drug\ in\ the\ vesicular\ complex}{vesicular\ complex\ weight}\right) * 100 \quad (2)$$

Analysis of the Drugs in the Samples

Stock solutions of xanthone and daclatasvir dihydrochloride (1000 µg/mL) were prepared by separately dissolving 10 mg of each drug in a 10 mL volumetric flask using distilled water as a solvent. Stock solution aliquots were further diluted with the same solvent before being scanned between 200 and 400 nm wavelength (Shimadzu - UV 1800 double beam UV-Visible spectrophotometer (Japan)) equipped with matched 1 cm quartz cells at 200–800 nm range, which were used for all absorbance measurements. Spectra were automatically obtained by Shimadzu UV-Probe 2.32 system software. Both drugs followed Beer's rule within the concentration range of 2–20 µg/mL.

To enable simultaneous determination, the absorption spectra of xanthone were divided by the spectrum of 6 µg/mL daclatasvir dihydrochloride, and vice versa, then the ratio spectra were differentiated to wavelength. The first derivative values (Δλ = 8.00, scale = 10) were plotted against the corresponding concentration, and the regression equation was calculated at 281 nm for xanthone and 300 nm for daclatasvir dihydrochloride.

Transmission Electron Microscopy

For morphological evaluation of the optimized formulated nanoparticles, transmission electron microscopy (JEM-1400 JEOL, Tokyo, Japan) was used. Lyophilized samples after hydration were pipetted onto copper grids, where a thin film was formed. The samples were stained with 10 µL droplet of 2% phosphotungestic acid solution and were allowed to dry for 10 s. After the staining step, any excess stain was rinsed off by briefly applying a 10 µL water droplet for 10 s [29].

in-vitro Drug Release

in-vitro release rate of xanthone and daclatasvir dihydrochloride were evaluated using dialysis bag method. Briefly, five preparations were tested; standard xanthone (0.8 mg pure xanthone in water), bilosomal dispersion of xanthone equivalent to 0.8 mg xanthone, standard daclatasvir dihydrochloride (5 mg pure daclatasvir dihydrochloride in water), CS-NPs dispersion of daclatasvir dihydrochloride equivalent to 5 mg daclatasvir dihydrochloride, and BCNP dispersion (containing 0.8 mg xanthone and 5 mg Daclatasvir dihydrochloride) were placed in the dialysis bag (Spectrum Medical Inc., Los Angeles, CA, USA, molecular weight cut

off 12,000–14,000 Da). The bags were then immersed in 50 mL phosphate buffer saline (PBS) at pH 7.4, in a thermostatically controlled mechanical shaker at 37 ± 0.50 °C at 50 rpm for 72 h. Different samples were withdrawn at time intervals 0, 0.166, 0.333, 0.5, 1, 2, 3, 4, 5, 6, 8, 24, 48 and 72 h, and replaced with fresh PBS to maintain sink conditions [29]. The goal was to compare the release profiles of both xanthone and daclatasvir dihydrochloride from the different carrier systems, either the single-component bilosomes or chitosan nanoparticles with the BCNP formulations. This allowed assessment of the impact of the bilosomes-chitosan nanoparticle formulation on controlling the release profiles of these two drugs [30].

Investigation of drug–excipient Interactions and Confirmation of Nanoparticle Formation Via Infrared Spectroscopy (FTIR)

Infrared spectroscopy was employed to evaluate possible interactions among the drugs, excipients, and the prepared nanoparticle formulations. To further confirm the association between bilosomes and chitosan nanoparticles, a Shimadzu IR spectrophotometer (Japan) was used with potassium bromide (KBr) pellets under ambient conditions (25 °C), operating in transmission mode. The analysis focused on detecting characteristic absorption bands within the spectral range of 4000 to 500 cm^{-1} [27].

Aerodynamic Properties Evaluation and Lung Deposition Modeling

Estimation of the Aerodynamic Diameter and the Geometric Standard Deviation

Due to the lack of direct in-vitro cascade impaction data, the Aerodynamic Diameter (AD) was estimated using Eq. 3 [31, 32].

$$AD = dv\sqrt{\frac{\rho_P}{\rho * X}} \tag{3}$$

Where dv is the geometric diameter (nm), ρ is the unit density = 1 g/cm^3, and X is the shape factor (spherical particles: X = 1), and ρp is the particle density (g/cm^3) which was be calculated from Eq. 4 [33].

$$\rho p = \frac{\sum_i Wi.\rho i}{\sum_i Wi} \tag{4}$$

Where Wi is the weight (or mass) fraction of component i, and Wi is true density of component i.

The Geometric Standard Deviation (GSD) was calculated from the polydispersity index using the approximation Eq. 5 [34].

$$GSD = exp\sqrt{ln\,(PDI + 1)} \tag{5}$$

Given that the GSD was found to be 1.75, the particle size distribution was assumed to be lognormal, allowing calculation of the mass median aerodynamic diameter (MMAD). First,

$$dmm = dv.exp\,(3ln^2.GSD) \tag{6}$$

Then, MMAD was calculated using Eq. 7 [35].

$$MMAD = dmm\sqrt{\frac{\rho_P}{\rho * X}} \tag{7}$$

Multiple Path Particle Dosimetry (MPPD) Modeling of Lung Deposition

The deposition pattern of the nanoparticles was simulated using MPPD v3.04, with the following input conditions: Exposure type: Constant, MMAD: 0.555 µm, GSD: 1.75, Density: 1.22 g/cm^3, Particle shape: Spherical, Breathing parameters: Human adult (nasal breathing), tidal volume: 625 mL, breathing frequency: 12 breaths/min, duty cycle: 0.5, Exposure duration: 1 h, Posture: Sitting. This simulation model was employed to estimate the regional deposition of nanoparticles within different compartments of the human respiratory tract, including the extrathoracic, tracheobronchial, and alveolar regions [36].

Stability Testing of the Optimized Formula

For stability testing, the lyophilized optimized formula (O_1) was stored at 5 °C ± 3 °C and 25 °C ± 2 °C/60% RH ± 5% for 6 months, and tested for any change in the particle size, polydispersity index, zeta potential and the EE% of both drugs at 1, 3 and 6 months time intervals, after hydration of the sample [37].

Antiviral Activity

MTT Cytotoxicity Assay

Stock solutions of the optimized formula (O_1) were prepared in 10% dimethyl sulfoxide (DMSO) (v/v) in double-distilled water. Two-fold serial dilution with Dulbecco's Modified Eagle Medium (DMEM) was done to obtain working

concentrations equivalent to (1–2000 µM) of daclatasvir dihydrochlride, for determining the half-maximal cytotoxic concentration (CC50). The cytotoxicity of the O_1 formula was assessed in VERO-E6 cells using a slightly modified 3-(4,5-dimethylthiazol-2-yl)−2,5-diphenyltetrazolium bromide (MTT) assay. Briefly, 100 µL of cell suspension, adjusted to a density of 3×10^5 cells/mL, were seeded into 96-well plates and incubated for 24 h at 37 °C with 5% CO_2. Following this incubation, cells were exposed to serial dilutions of the O_1 formula in triplicate. After 24 h of treatment, the supernatant was removed, and the cell monolayers were washed three times with sterile 1X phosphate-buffered saline (PBS) to eliminate residual components. Subsequently, 20 µL of MTT solution (5 mg/mL stock) was added to each well, and the plates were incubated at 37 °C for 4 h. Following incubation, the medium was aspirated, and the resulting formazan crystals were dissolved using 200 µl of acidified isopropanol (0.04 M HCl in absolute isopropanol) per well.

The absorbance of the formazan solutions was measured at 540 nm, with 620 nm as a reference wavelength, using a multi-well plate reader [38]. The percentage of cell viability of the optimized formula (O_1) treated cells was calculated relative to untreated control cells using Eq. 8.

$$\%\ cytotoxicity = \frac{absorbance\ of\ cells\ without\ treatment - absorbance\ of\ cells\ with\ treatment}{absorbance\ of\ cells\ without\ treatment} \times 100 \quad (8)$$

50% cytotoxicity CC_{50} and IC_{50} values were determined using nonlinear regression analysis. Sample concentrations were log-transformed and fitted to a four-parameter logistic (4PL) nonlinear regression model in GraphPad Prism software (version 9.5.1). Responses were normalized against untreated control wells to define 100% viability or infection. Both IC_{50} and Inhibitory concentration 50 (CC_{50}) were interpolated from the fitted sigmoidal dose–response curves [39].

Inhibitory Concentration 50 (IC_{50}) Determination

In 96-well tissue culture plates, Vero-E6 cells (2.4×10^4 cells per well) were seeded and incubated overnight in a humidified incubator at 37 °C with 5% CO_2. The resulting cell monolayers were washed once with 1X PBS and subsequently exposed to virus adsorption (hCoV-19/Egypt/NRC-03/2020; GSAID Accession Number: EPI_ISL_430820) for 1 hat room temperature (RT) [40]. The cell monolayers were subsequently overlaid with 100 µL of serum-free DMEM containing different concentrations of the optimized formula (O_1). After incubating the cells for 72 h at 37 °C in a 5% CO_2 incubator, they were fixed with 100 µL of 4% paraformaldehyde for 20 min. The cells were then stained with 0.1% (w/v) crystal violet in distilled water for 15 min at room temperature. The optical density of the dye was measured at 570 nm using an Anthos Zenyth 200rt plate reader (Anthos Labtec Instruments, Heerhugowaard, Netherlands). The crystal violet stain was dissolved by adding 100 µL of 100% methanol per well. The IC_{50} value was defined as the concentration of the compound required to reduce the virus-induced cytopathic effect (CPE) by 50% compared to the virus control [40].

In-vivo Pharmacodynamics Study

Experimental Animals

Thirty male C57BL/6 mice (aged 8 weeks, 15–20 g) were obtained from the Egyptian Company for Production of Vaccines, Sera and Drugs (EGYVAC; Cairo, Egypt). Mice were kept in plastic cages under constant conditions of temperature 25 ± 3 ◦C and humidity 50% and allowed free access to water and standard pellet chow at the animal house of October University for Modern Sciences and Arts (MSA). The study was approved by the ethics committee of MSA University (Approval number PT3/Ec3/2022PD).

Experimental Design

Sample size determination was performed using GPower software, based on expected differences in serum surfactant protein levels, with the statistical power set at 80%. Thirty mice were randomly assigned to five experimental groups ($n = 6$ per group) using random numbers generated via the standard = RAND() function in Microsoft Excel. The experimental groups included:

Group I Normal control mice.

Groups II (LPS) Mice induced with acute respiratory distress syndrome (ARDS), after being injected with LPS 15 mg/kg [41].

Group III (B + LPS) Mice received the blank formulation for 7 days and the mice were induced with ARDS by injecting them with LPS on the last day of the experiment.

LPS, a constituent of the outer membrane of Gram-negative bacteria, was employed to induce acute respiratory distress syndrome (ARDS) due to its well-characterized ability to elicit a pronounced systemic inflammatory response. This model reliably reproduces key pathological features of ARDS, including cytokine storm and acute lung injury, thereby serving as a robust platform for evaluating the anti-inflammatory and pulmonary protective efficacy of the test formulation [42].

Group IV (XD + LPS) Mice were treated daily with standard xanthone (xanthone in water) (2 mg/kg) and standard daclatasvir (daclatasvir in water) (6 mg/kg) via nebulizer for 7 days and injected with LPS at day 7. The dose of xanthone was determined based on a previous study [39, 43–47].

Group V (XDF + LPS) Mice were treated daily with the formulation of xanthone and daclatasvir via nebulizer for 7 days and injected with LPS at day 7.

At the end of the treatment period, mice were euthanized under ether anesthesia 6 h after receiving an LPS injection. The lungs were promptly removed and rinsed with ice-cold saline. The right lungs were stored at −80 °C for biochemical analysis, while the left lungs were fixed in a 10% formalin solution for histopathological examination. To minimize bias, sample collection from each mouse was performed by one investigator, while all subsequent biochemical and molecular analyses were conducted by a second investigator who was blinded to the group assignments.

Biochemical Investigations

PromoCell's ACE2 activity assay kit was employed to evaluate ACE2 activity in lung tissue, following the manufacturer's protocol (PromoCell, Heidelberg, Germany) and using a fluorescence microplate reader (Thermo Fisher Scientific Oy, FI-01621 Vantaa, Finland). Pulmonary surfactant protein-1 (SP-1) levels were determined using the ELISA technique with a standard kit (Cloud-Clone Corp., TX, USA). Additionally, standard ELISA kits were utilized to measure pulmonary levels of angiotensin 1–7 and angiotensin II (Abbexa Ltd, Cambridge, UK, and LifeSpan Biosciences, Inc.) as well as nuclear factor-κB (NF-κB) and tumor necrosis factor-α (TNF-α). Absorbance was recorded (OD range: 490–630) with an ELISA plate reader (Stat Fax 2200, Awareness Technologies, Miami, FL, USA).

Total RNA was extracted from lung tissue samples using Trizol (Invitrogen) in accordance with the manufacturer's guidelines and subsequently reverse-transcribed into cDNA using Reverse Transcriptase M-MLV (Promega, Madison, WI, USA). A 96-well StepOne instrument (Applied Biosystems, USA) was used for analysis, with data expressed as Cycle threshold (Ct) values for both the target gene and housekeeping gene. The primer sequences used in the experiment were as follows:

Gene	Forward primer	Reverse primer
GAS5	CACGTGTTCCATCCTGGTC A**X67268.1**	GTCAAGGAAG CCCACCATCA
β-actin	CGTTGACATCCGTAAAGA C**NM_007393.5**	TGGAAGGTGG ACAGTGAG

Immunohistochemical Assessment of TNF-α

For immunohistochemical staining, deparaffinized tissue sections underwent antigen retrieval and were treated with 0.3% H_2O_2 for 20 min. The samples were then washed and incubated with an anti-TNF-α polyclonal antibody (Abcam, dilution 1:100). Following this, they were washed again and treated with a secondary antibody using the HRP Envision kit (DAKO) for 20 min. After washing with PBS, the sections were incubated with diaminobenzidine (DAB) for 10 min and prepared for examination under a light microscope. Five representative non-overlapping fields were randomly selected and analyzed per tissue sample to determine the percentage area of TNF-α immunohistochemical expression based on the density and distribution of brown staining.

Histological Examination of Lung Tissue

Lung tissues from groups I to V were fixed in 10% neutral buffered formalin solution for 72 h. Samples were then washed in Xylene, trimmed and processed in serial grades of alcohols, infiltrated, and implanted into Paraplast tissue embedding media. Tissue sections approximately 5 n thick were cut using a rotatory microtome and stained with H&E for histological examination under a light microscope (Leica Microsystems GmbH, Wetzlar, Germany) [48].

Statistical Analysis

Data analysis and optimization were conducted using Design-Expert® 13.0.5.0 software (Stat-Ease Inc., USA), following analysis of variance (ANOVA). Antiviral and pharmacodynamic study results were expressed as mean ± standard error of the mean (SEM). Group mean comparisons were performed using one-way ANOVA followed by Tukey-Kramer's multiple comparisons test. The Kruskal–Wallis test was used to analyze histopathological scores, followed by Dunn's multiple comparisons test. A $p < 0.05$ was considered statistically significant. All statistical analyses were performed using GraphPad Prism (version 9.5.1) (GraphPad Software Inc., USA).

Results and Discussion

Preparation of bilosome-chitosan Nanoparticles

Lipid-based formulation made from bilosomes ionically cross-linked with chitosan nanoparticles were developed in the current study. The goal was to attach the bilosomes to the surfaces of the chitosan nanoparticles, resulting in the

formation of a lipid coating or a shell surrounding the chitosan nanoparticle surfaces.

BCNP system was fabricated using a technique that involved coating the formed chitosan nanoparticles with the bilosomal vesicles coat. Specifically, this coating was achieved by rehydrating a freeze-dried mixture of chitosan nanoparticles and bilosomes. The theoretical basis for the construction of this nanosystem is that the positively charged CS-NPs interact with the negatively charged bilosomal vesicles. This interaction induces a reorganization of the bilosomal membranes, allowing them to envelop the surface of the nanoparticles and form bilosomes-coated chitosan nanoparticles [22].

The developed bilosome–chitosan nanoparticle (BCNP) system addresses several limitations associated with traditional liposomes, such as relatively rapid clearance by macrophages in the reticuloendothelial system [49, 50], low therapeutic efficacy; as liposomes can suffer from drug leakage during storage or after administration due to lipid bilayer instability [51, 52], and restricted permeability across biological membranes [53, 54], as well as challenges with chitosan nanoparticles alone, including the rapid release of hydrophilic drugs [55, 56]. By combining both carriers, this complex system enhances versatility and improves interaction with biological surfaces and cellular membranes, thereby facilitating targeted drug delivery to specific tissues, and significantly improves therapeutic performance by increasing drug bioavailability and stability [22].

Chitosan's mucoadhesive and permeability-enhancing characteristics support prolonged retention and efficient drug transport across mucosal surfaces, especially in the lungs [19]. These nanoparticles can boost the effectiveness of antiviral agents. They also improve drug penetration through the mucus barrier, increase the drug's anti-inflammatory effects, and promote increased uptake or interaction with specific cells, such as macrophages [21, 57]. Meanwhile, the bilosomal coating acts as a protective reservoir that enables controlled and sustained drug release, maintaining a steady therapeutic concentration at the site of infection and inflammation [16].

It is proposed that coating the surface of prefabricated CS-NPs or embedding them within the lipidic bilayers of the bilosomes, create an innovative mixture capable of simultaneously delivering both hydrophilic and hydrophobic drugs for combination therapy [58]. This nanoparticle-based co-delivery system may reduce dosing frequency and systemic toxicity by localizing the drug's action. The ability to co-encapsulate both hydrophobic (e.g., xanthone) and hydrophilic (e.g., daclatasvir) drugs within a single carrier also simplifies treatment regimens. This is particularly valuable in diseases like COVID-19, where simultaneous control of viral replication and inflammation is crucial.

It is worth mentioning that the incorporation of bile salt as sodium deoxy cholate with liposomes could stabilize the liposomal membrane and fluidize lipid bilayers and disrupt tight junctions in epithelial tissues [57, 59]. Its incorporation into liposomes improves drug permeability across respiratory mucosa, making it easier for the encapsulated drugs to penetrate deep lung tissue. Furthermore, it induces a stronger negative charge on the liposomal bilayer [60], hence improves its interaction with the chitosan nanoparticles for better ionic cross-linking with chitosan nanoparticles. Additionally, the bile salt also aids in preventing mucus entrapment by improving mucus penetration, which is particularly beneficial in conditions like ARDS [61].

The combination therapy using bilosome-chitosan nanoparticles represents a significant advancement over conventional COVID-19 and ARDS therapies by addressing two critical limitations of current approaches: the inefficient lung-specific drug delivery in addition to the uncontrolled inflammation. While existing treatments like remdesivir (systemic) or dexamethasone (broad immunosuppression) suffer from off-target effects and variable lung bioavailability [62], the optimized nanoparticle system with charge-mediated mucoadhesion is proposed to enable precise alveolar deposition [63]. The system's ability to co-deliver xanthone (anti-inflammatory/antiviral) and daclatasvir (antiviral) synergistically could target both viral replication (via NS5A inhibition) and cytokine storm (via NF-κB suppression). This approach aligns with emerging trends in inhaled nanomedicine for ARDS [64], offering a scalable alternative to monoclonal antibodies or repurposed antivirals with narrow therapeutic windows [65].

FT-IR Analysis

As can be observed from Fig. 1a, which presents the IR spectrum of daclatasvir dihydrochloride, characteristic bands are observed at 3383.1 and 3149.76 cm^{-1}, corresponding to N–H stretching vibrations, supporting the presence of the N–H functional groups. A strong absorption band at 1726.29 cm^{-1} indicates the presence of a carbonyl group, likely situated between amide and ester moieties. Additionally, the band at 1645.29 cm^{-1} may be attributed to another carbonyl stretch associated with amide groups. the presence of a carbonyl group, likely situated between amide and ester moieties. Additionally, the band at 1645.29 cm^{-1} may be attributed to another carbonyl stretch associated with amide groups [66]. The IR spectrum of chitosan (Fig. 1b) exhibits a prominent absorption peak at 3423.71 cm^{-1}, which can be attributed to O–H and N–H stretching vibrations. A band at 2923.17 cm^{-1} corresponds to C–H stretching. Whereas, the band at 1651.09 cm^{-1} is indicative of C = O stretching from amide groups, while

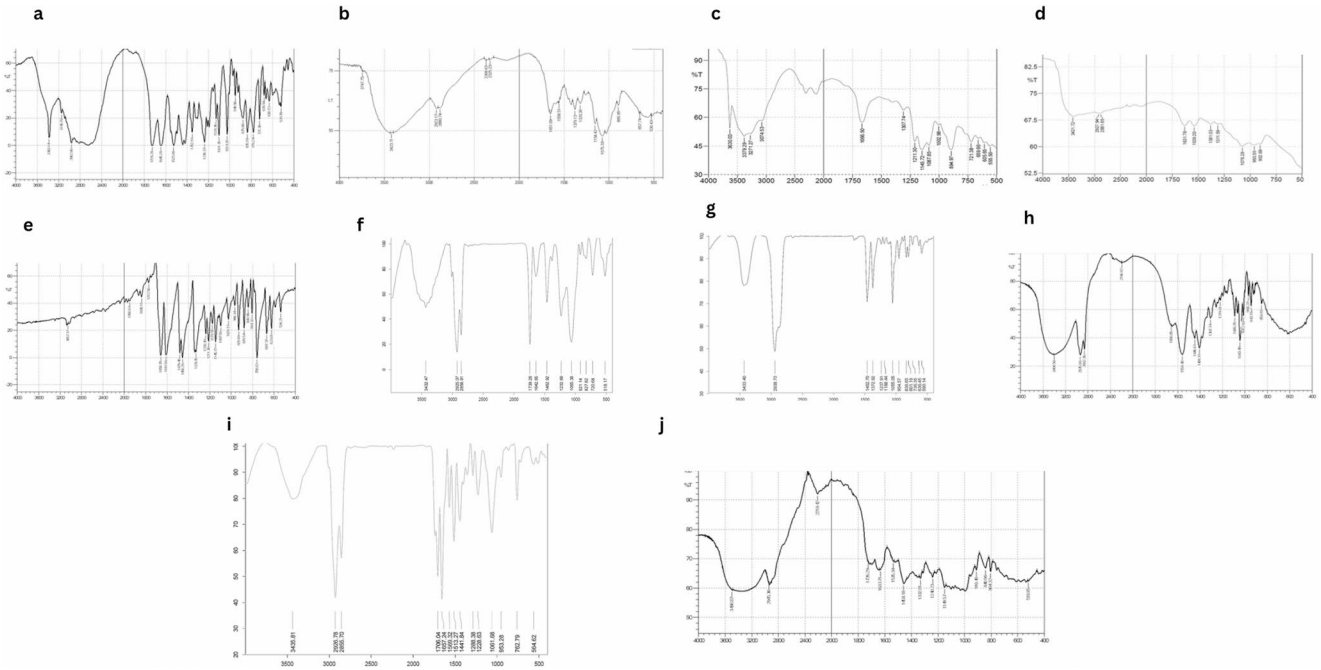

Fig. 1 FT-IR spectrum of (**a**) Daclatasvir Dihydrochloride, (**b**) Chitosan, (**c**) Tripolyphosphate, (**d**) CS-NPs, (**e**) Xanthone, (**f**) SoyPhosphatidyl Choline, (**g**) Cholesterol, (**h**) Sodium deoxycholate, (**i**) Bilosomes, and (**j**) BCNP

the absorption at 1558.1 cm^{-1} is associated with N–H bending vibrations. Additional bands observed at 1379.13 cm^{-1} and 1075.53 cm^{-1} could be attributed to C–H stretching in CH_2OH groups and C–O stretching in CH–OH, respectively. The TPP spectrum as can be deduced from Figure 1c shows characteristic bands in the 1211.30–1087.85 cm^{-1} region, attributed to P = O stretching vibration, and a peak at 894.97 cm^{-1} corresponding to P–O bonds, indicating the phosphate backbone. The IR spectrum of chitosan nanoparticles (CS-NPs), shown in Fig. 1d, exhibits a broad and intense band at 3421.72 cm^{-1}, attributed to overlapping –OH and $–NH_2$ stretching vibrations of chitosan, as well as interactions between the phosphate groups of TPP and the $–NH_2$ groups of chitosan [67]. This broadening may also reflect hydrogen bonding between chitosan and daclatasvir, suggesting possible intermolecular interactions [68]. The band at 1631.78 cm^{-1} corresponds to the C = O stretching, while 1539.20 cm^{-1} relates to the N–H bending vibration of the amide II band, where shifts in these peaks compared to pure chitosan suggest the potential involvement of these functional groups in electrostatic interactions or hydrogen bonding with daclatasvir [68]. The absorption bands at 1381.03 cm^{-1} and 1311.59 cm^{-1} are linked to C–N stretching and CH_2 wagging vibrations, respectively. Meanwhile, the peaks around 1076.28 cm^{-1}, 960.55 cm^{-1}, and 902.69 cm^{-1} are characteristic of C–O–C and P–O stretching, typically found in chitosan phosphate crosslinked systems. These bands further support the polysaccharide structure and confirm the formation of crosslinked nanoparticles via ionic gelation [69]. Notably, no distinct peaks attributable solely to daclatasvir dihydrochloride were observed in the nanoparticle spectrum, implying that either the drug was molecularly dispersed or involved in strong interactions with the chitosan matrix.

As can be deduced from Fig. 1e, the spectrum of xanthone shows a strong absorption band at 1658.78 $cm^{-1}$and 1610.56 cm^{-1} which could be attributed to the stretching vibrations of C = C and C = O bonds within the conjugated aromatic and carbonyl systems, respectively. These bands are consistent with the α-pyrone ring and aromatic ketone structure of xanthone [70].

The FTIR spectrum of soy phosphatidylcholine (Fig. 1f) displays several prominent peaks confirming its phospholipid structure. A strong peak around 2925 cm^{-1} corresponds to the asymmetric C–H stretching of $–CH_2$ groups. A distinct peak was observed at 1739.28 cm^{-1}, which is attributed to the ester carbonyl (C = O) stretching vibration, a characteristic feature of the phospholipid glycerol backbone. Additionally, a peak near 1230–1080 cm^{-1} corresponds to P = O and P–O–C stretching, confirming the presence of phosphate head groups [27]. The spectrum of cholesterol (Fig. 1g) exhibited a broad O–H stretching band around 3432.47 cm^{-1}, which is indicative of the hydroxyl group. The prominent peaks at 2925.07 cm^{-1} and 2856.91 cm^{-1} are assigned to the asymmetric and symmetric C–H stretching vibrations of aliphatic chains. The band observed at 1462.95 cm^{-1} corresponds to CH_2 bending, while the peak around 1065.38 cm^{-1} may relate to C–O

stretching from the secondary alcohol group [71]. The spectrum of sodium deoxycholate (Fig. 1h), shows a broad O–H stretching band around 3400.5 cm^{-1}, suggesting the presence of multiple hydroxyl groups. Peaks at 2965.66 cm^{-1} and 2862.36 cm^{-1} indicate aliphatic C–H stretching. The bands around 1600–1550 cm^{-1} likely reflect COO^- asymmetric stretching from the carboxylate salt form. Peaks between 1200 and 1000 cm^{-1} correspond to C–O stretching and bending of hydroxyl groups present in the bile salt structure [72]. The spectrum of the bilosome formulation reveals key peaks consistent with the combined contributions of phosphatidylcholine, cholesterol, and sodium deoxycholate. The merged C–H stretching peaks at 2925 cm^{-1} and 2852 cm^{-1}, along with a prominent ester C = O stretch around 1736 cm^{-1}, confirm the lipid vesicle formation. P = O stretching at 1228.38–1061.68 cm^{-1} remains visible, and a reduction in the intensity of the O–H region may suggest partial hydrogen bonding or encapsulation effects among bilayer components [73]. Notably, the typical C = O and C = C peaks of xanthone, usually observed around 1650–1600 cm^{-1}, appear to overlap with the bilosome peaks, indicating successful encapsulation. The absence of sharp, separate xanthone signals suggests that the drug is well incorporated within the lipid bilayer, possibly through hydrophobic and hydrogen bonding interactions. Peaks between 1230 and 1080 cm^{-1} (P = O and P–O–C stretches) remain visible and are associated with the phospholipid head groups.

The bilosome–chitosan complex spectrum as deduced from Fig. 1j, shows significant broadening in the O–H/N–H region near 3400 cm^{-1}, indicative of hydrogen bonding between chitosan and the bilayer surface. The characteristic lipid peaks (C–H stretches at 2920 cm^{-1}, ester C = O at 1730 cm^{-1}) are retained, but with slight shifts or reduced intensity, suggesting surface interactions rather than disruption of the lipid bilayer. Importantly, new features emerge in the 1640–1540 cm^{-1} region, which correspond to N–H bending and possible interactions between the amino groups of chitosan and the phosphate or carboxylate groups of bilosomal lipids. The band near 1100 cm^{-1} corresponds to C–O and P–O stretching, further supporting the formation of a polyelectrolyte complex.

These spectral changes confirm the successful coating of bilosomes with chitosan nanoparticles, resulting in a stable lipid–polymer system.

Analysis of the Drugs

The absorption spectra of both drugs overlapped closely as shown in Figure 2a. For this reason, direct measurement of

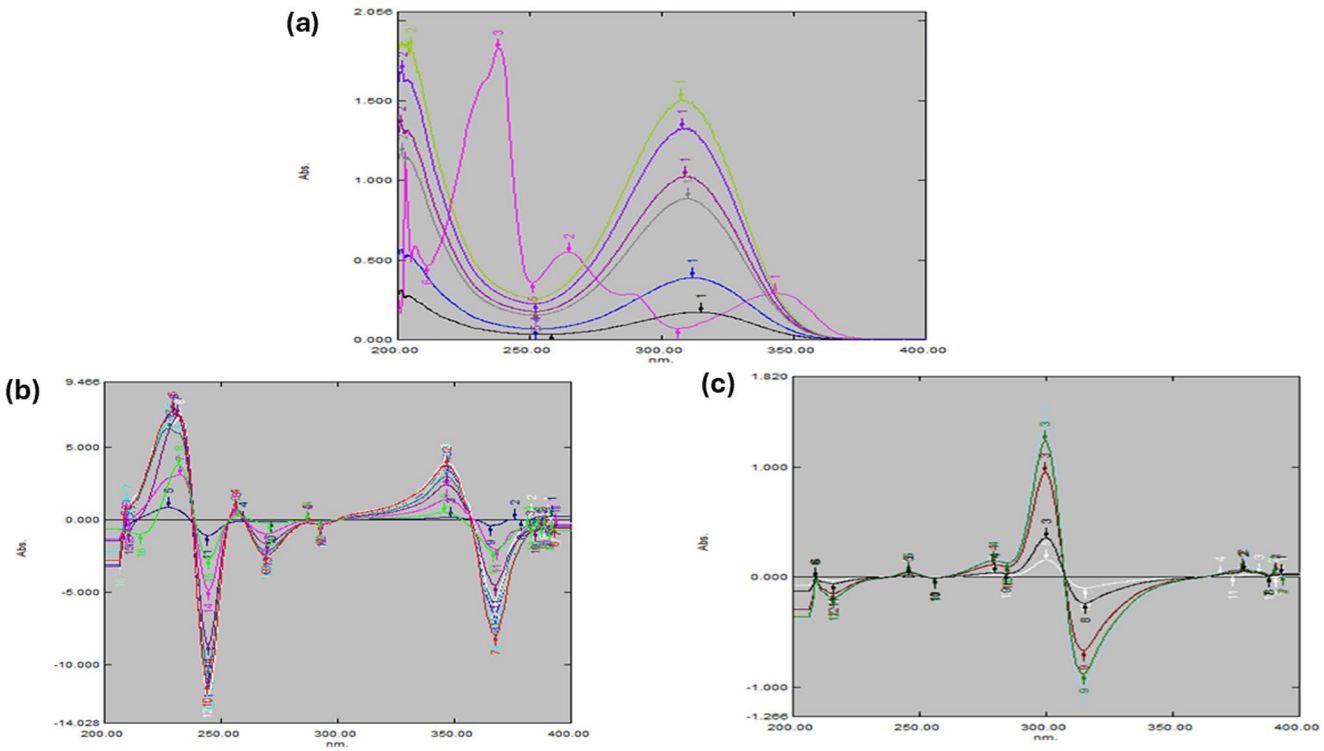

Fig. 2 (**a**) Overlapped zero-order spectra of xanthone and daclatasvir dihydrochloride, (**b**) first order of derivative ratio spectra of xanthone 2-20 µg/mL using 6 µg/mL of daclatasvir dihydrochloride as a divisor and (**c**) first order of derivative ratio spectra of daclatasvir dihydrochloride 2-20 µg/mL using 6 µg/mL of xanthone as a divisor

absorbance in zero-order spectra was not possible. However, spectrophotometric techniques based on the derivative approach demonstrated a higher resolution and allowed for the analysis of each individual drug when present in combination [74].

To optimize the first derivative method, various divisor concentrations (3, 6, and 9 µg/mL) were evaluated, with the optimal result achieved using 6 µg/mL as the divisor. Different smoothing and scaling factors were also tested, and a smoothing factor of $\Delta\lambda = 8$ along with a scaling factor of 10 proved effective for enhancing the signal, simplifying measurement, and reducing reading errors. The resulting ratio spectra are depicted in Fig. 2b and c. The DD1 values exhibited excellent linearity and reproducibility at 281 nm for xanthone and 300 nm for daclatasvir dihydrochloride (Table 2), with the corresponding linear regression equations provided in Eqs. 9 and 10.

$$y = -0.048\ C1 + 0.0142 \tag{9}$$

$R^2 = 0.9970$, at 281 nm for xanthone.

$$y = 0.522\ C2 - 0.0508 \tag{10}$$

$R^2 = 0.9963$, at 300 nm for daclatasvir dihydrochloride, where C_1 is xanthone concentration and C_2 is daclatasvir dihydrochloride concentration.

Optimization by One Factor Design

The results of the prepared formulations, the desired constraints together with the characterization tests results used in the optimization step are presented in Table 1.

Table 2 Validation sheet for the proposed spectrophotometric method for the quantification of Xanthone and 300 nm for Daclatasvir dihydrochloride

Parameter		Xanthone	Daclatasvir
λmax (nm)		281	300
Linearity range (µg /mL)		2-20	0.4-3.8
Correlation coefficient (r)		0.9970	0.9963
Slope		0.048	0.522
Intercept		0.0142	-0.0508
LOD [a] (µg /mL)		0.104	0.094
LOQ [a] (µg /mL)		0.312	0.287
Accuracy [b] (Recovery %±SD)		99.73 ± 1.11	99.97 ± 1.28
Precision [c] (%RSD)	Intra-day	1.43	0.91
	Inter-day	1.94	1.77

[a]LOD= (S.D of the response/slope) × 3.3; LOQ= (S.D of the response/slope) × 10

[b]The average of three experiments

[c]The average of nine experiments

Particle Size Analysis

The particle size of the bilosome-chitosan complex formulations ranged from 200 ± 10.5 to 280 ± 16.9 nm, as observed from Table 1, which is considered optimal for drug delivery applications. Particles within this size range facilitate cellular uptake through passive transport mechanisms, enabling effective drug delivery into the cells [75].

Further analysis using ANOVA (Table 3) revealed that particle size was a statistically significant response, as indicated by a $p < 0.05$, along with an insignificant lack of fit. The best-fitting model for particle size was identified as a quartic model. Notably, the difference between the adjusted R^2 (0.9976) and the predicted R^2 (0.9960) was less than 0.2, and the model exhibited an adequate precision value of 99.48. These metrics indicate that the model is reliable and can be effectively used to navigate the design space.

The relationship between the ratio of bilosomes: CS-NPs and the particle size is clearly defined by the regression equation as represented in Eq. 11. As can be observed from Eq. 11, an increase in this ratio resulted in an increase in particle size, as indicated by the positive coefficient associated with X_1. This phenomenon could be attributed to the increase in lipidic content due to the bilosome increase, by increasing this ratio, with the subsequent increase in the hydrophobicity of the nanoparticles system, leading to a decrease in the binding affinity (attractive force) between the bilosomes and the positively charged chitosan. Consequently, the structure of the nanoparticles may become more loosely bound, resulting in an increase in particle size [76].

$$\text{Particle Size} = +201.00 + 51.96 * X_1 + 313.70 * X_1^2 - 65.03 * X_1^3 - 270.80 * X_1^4 \tag{11}$$

However, due to the quartic nature of the model, the effect of changing the bilosome: CS-NPs ratio on the vesicular size followed a non-linear relationship as presented in Figure 3a. An increase in the vesicular size was observed as the ratio increased from 1:1 to 1.25:1, which was followed by a decrease in size up to a ratio of 2:1. A further increase in the bilosome: chitosan till 2.75: 1 resulted in a larger vesicular size, whereas when the ratio reached to 3:1 the particles were smaller in size. The smallest particle size was achieved at a ratio of 2:1, which is particularly favorable for deeper lung and alveolar deposition; which is critical for targeting acute respiratory distress syndrome (ARDS), while minimizing deposition in the upper respiratory tract [77].

Table 3 ANOVA study of the studied responses

Source	PS (nm) (Quartic)					ZP (mv) (Quartic)					EE% of Xanthone (Quartic)					EE% of Daclatasvir dihydrochloride (Quartic)				
	Sum of Squares	df	Mean Square	F-value	*p*-value	Sum of Squares	df	Mean Square	F-value	*p*-value	Sum of Squares	df	Mean Square	F-value	*p*-value	Sum of Squares	df	Mean Square	F-value	*p*-value
Model	7697.51	4	1924.38	1256.37	<0.0001	107.05	4	26.76	126.82	<0.0001	403.69	4	100.92	110.74	<0.0001	372.11	4	93.03	187.10	<0.0001
X_1-Bilosomes: CSNPs	1506.79	1	1506.79	983.74	<0.0001	76.35	1	76.35	361.83	<0.0001	1.63	1	1.63	1.79	0.2179	0.7907	1	0.7907	1.59	0.2428
X_1^2	5014.40	1	5014.40	3273.76	<0.0001	3.40	1	3.40	16.12	0.0039	132.23	1	132.23	145.09	<0.0001	37.86	1	37.86	76.14	<0.0001
X_1^3	2114.67	1	2114.67	1380.60	<0.0001	95.01	1	95.01	450.24	<0.0001	28.17	1	28.17	30.91	0.0005	29.20	1	29.20	58.72	<0.0001
X_1^4	4782.56	1	4782.56	3122.40	<0.0001	2.91	1	2.91	13.80	0.0059	134.77	1	134.77	147.89	<0.0001	38.63	1	38.63	77.69	<0.0001
Residual	12.25	8	1.53			1.69	8	0.211			7.29	8	0.9113			3.98	8	0.4972		
Lack of Fit	2.78	4	0.6959	0.2939	0.8686	0.8472	4	0.212	1.01	0.4973	2.26	4	0.5645	0.4487	0.7716	1.35	4	0.3373	0.5133	0.7329
Pure Error	9.47	4	2.37			0.8410	4	0.210			5.03	4	1.26			2.63	4	0.6571		
Cor Total	7715.30	13				108.75	13				410.98	13				378.37	13			

Zeta Potential Analysis

The negative charge of the formed nanoparticles could be due to the bilosomal vesicles' coat and its impact on imparting the negative charge due to the phosphatidyl choline together with the sodium deoxycholate, and confirms the embedding of the chitosan nanoparticles within the lipidic bilayer of the bilosomes [75].

The value of the ZP ranged from − 10 ± 1.6 mV to −19 ± 2.6 mV, as represented in Table 1. It has been reported that a well-stabilized nanoparticles system could have a zeta potential value from ± 15 to ± 50mV [30]. Thus, the zeta potential would be optimized for the maximum stability of the system.

ANOVA results for the ZP, as presented in Table 3, indicate that the study of zeta potential was statistically significant, as evidenced by the $p < 0.05$. Additionally, the data revealed that the best fitting model for the zeta potential was a quartic model. Statistical analysis showed that the adjusted R^2 (0.9767) was in reasonable agreement with the predicted R^2 (0.9430) (difference less than 0.2), with an adequate precision of 27.61. These findings suggested that the model can be reliably used to explore the design space.

The relationship between the ratio of bilosomes: CS-NPs and the ZP is clearly defined by the regression equation as represented in Eq. 12.

$$ZP = +16.00 + 11.70 * X_1 - 8.17 * X_1^2 - 13.78 * X_1^3 + 6.68 * X_1^4 \quad (12)$$

As can be observed, an increase in the ratio of bilosomes: CS-NPs resulted in an increase in the absolute zeta potential, as indicated by the positive coefficient associated with X_1. This effect is likely due to the increase in the bilosome content as the ratio increases, which subsequently increases the negative charge on the surface of the bilosomes. Simultaneously, the amount of positively charged chitosan nanoparticles decreases. This resulted in an increase in the absolute value of the negative zeta potential. However, as shown in Fig. 3b, this quartic effect was evident only within the bilosome: CS-NPs ratio range of 1.5:1 to 2.5:1, with the highest zeta potential observed at a ratio of 2.5:1. In contrast, at ratios lower than 1.5:1 or higher than 2.5:1, increasing the bilosome: CS-NPs ratio led to a decrease in the absolute zeta potential value.

Entrapment Efficiency of Xanthone Analysis

The EE% of xanthone within the bilosomal vesicles ranged from 79 ± 3.8% to 90 ± 2.8% as deducted from Table 1. The high value of entrapment efficiency of xanthone could be due to its hydrophobic nature and the capability of the

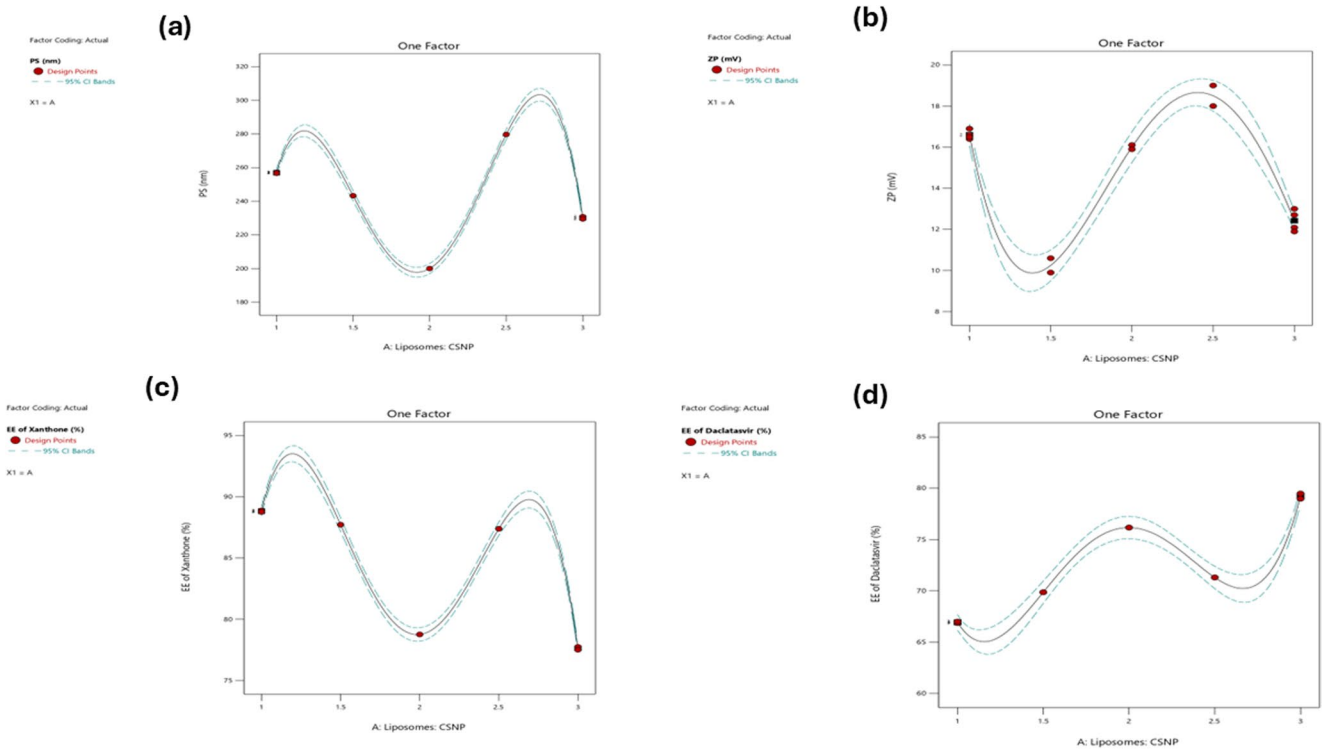

Fig. 3 One factor plot of the effect of changing bilosome CS-NPs ratio on the (**a**) particle size, (**b**) zeta potential, (**c**) entrapment efficiency of xanthone, and (**d**) entrapment efficiency of daclatasvir dihydrochloride

bilosomal vesicles to enclose hydrophobic drugs [15]. The EE% of xanthone was further analyzed with ANOVA study as represented in Table 3. The model was found to be a quartic significant model with an insignificant lack of fit. The adjusted R^2 (0.9734) was in close agreement with the predicted R^2 (0.9470), with an adequate precision of 18.60. Thus, the model was validated to navigate the design space.

The regression equation representing the relationship between the bilosome: CS-NPs and the EE% of xanthone is presented in Eq. 13. As can be observed from the positive coefficient of X_1, that increasing the bilosome: CS-NPs ratio resulted in an increase in the EE% of xanthone. Probably this is due to increasing the bilosome amount that encloses the xanthone which eventually result in increasing the EE% of xanthone [78]. However, a non-linear relation between the studied factor and the EE% of xanthone could be observed in Fig. 3c, which reveals that this effect was obvious when the ratio was 1:1 till 1.25:1, with the highest value at the ratio of 1.25:1, and from 2:1 till 2.75:1 only.

$$\text{EE\% of X} = +77.88 + 1.71 * X_1 + 50.94 * X_1^2 - 7.51 * X_1^3 - 45.46 * X_1^4 \quad (13)$$

Entrapment Efficiency of Daclatasvir Dihydrochloride Analysis

Daclatasvir dihydrochloride within chitosan nanoaprticles showed an entrapment efficiency of 67 ± 1.5 to 80 ± 2.7% as represented in Table 1. Being a hydrophilic drug, belonging to BCS class I [79], daclatasvir dihydrochloride showed a good entrapment efficiency in chitosan nanoparticles, as chitosan is a hydrophilic polymer that can easily encapsulate hydrophilic drugs [80]. Further analysis of EE% of daclatasvir dihydrochloride using ANOVA (Table 3) revealed a quartic significant model, with insignificant lack of fit. Moreover, a close agreement was observed between the adjusted R^2 (0.9841) and the predicted R^2 (0.9715), with an adequate precision of 29.7. Thus, this model could be used to navigate the design space.

The relationship between the bilosome: CS-NPs and the EE% of daclatasvir dihydrochloride is presented in the linear regression Eq. 14. The negative coefficient of X_1, reveals that increasing the bilosome: CS-NPs ratio resulted in a diminished EE% of the hydrophilic drug daclatasvir dihydrochloride. The reason behind this could be attributed to the reduction in the chitosan nanoparticles by increasing the bilosome: CS-NPs ratio, with the consequence of

reduction of incorporation of daclatasvir dihydrochloride to the nanoparticles system. As shown in Fig. 3d, this effect was observed only within the bilosome: CS-NPs ratio ranges of 1:1 to 1.25:1 and 2:1 to 2.75:1, consistent with the quartic model indicating a four-level interaction. Notably, the highest entrapment efficiency of daclatasvir dihydrochloride was recorded at a ratio of 3:1. This may be attributed to the increased amount of bilosomes available at that ratio, allowing for greater encapsulation of chitosan nanoparticles.

$$\text{EE\% of D} = +75.58 - 1.19 * X_1 - 27.26 * X_1^2 + 7.64 * X_1^3 + 24.34 * X_1^4 \quad (14)$$

Optimization of BCNP

Design-Expert 13.0.5.0 software was used for numerical optimization based on desirability index, with the target of the least particle size (in the range of 50 to 500 nm), the maximum absolute value of zeta potential, and the highest entrapment efficiency of both drugs. An optimized formula (O_1) was suggested by the software based on the desired constraints with a desirability of 0.591, which was prepared and tested in terms of the previously mentioned tests to compare the expected results with the observed results, to calculate the %bias as represented in Table 4 [81]. As can be observed, the validity of the design was established due to the low values of % bias [27].

The bilosome-xanthone nanoparticles (PS = 167 ± 2.5 nm, ZP = −24.6 ± 1.4 mV) and chitosan-daclatasvir nanoparticles (PS = 93 ± 1.8 nm, ZP = + 15 ± 0.4 mV) each present limitations for pulmonary delivery when administered separately. While the bilosomal system's negative charge provides colloidal stability, its sub-200 nm size results in an aerodynamic diameter ($d_a \approx 0.17$ µm) prone to alveolar exhalation (>80% exhaled for particles < 0.3 µm). Conversely, the chitosan nanoparticles' positive charge enhances mucoadhesion but their sub-100 nm size leads to near-complete exhalation. The formulated complex (PS = 222.67 ± 14.4 nm, ZP = −19.10 ± 3.7 mV) demonstrates critical improvements: firstly, its intermediate size yields a calculated $d_a \approx 0.23$ µm, which could result in a larger MMAD [82], for alveolar deposition through enhanced sedimentation. Moreover, the balanced surface charge maintains sufficient stability while preserving chitosan's mucus-binding capacity through localized positive charge domains [83]; furthermore, the combined architecture combines bilosomal protection of xanthone with chitosan's sustained release of daclatasvir. Importantly, the sytem's size distribution avoids both rapid mucociliary clearance (>500 nm) and macrophage uptake (< 200 nm), while its moderate negative charge reduces opsonization risks compared to strongly positive systems [84]. This synergistic optimization of physical and surface properties could result in a greater lung retention compared to individual components, making it particularly advantageous for combinatorial pulmonary therapy.

in-vitro Release Rate Study

A comparative in-vitro release study was conducted to evaluate the drug release profiles of each compound in its unformulated (standard) form, when incorporated into individual nanoparticle systems, and finally within the mixture BCNP formulation (Fig. 4). The objective was to investigate how nanoparticle encapsulation, and particularly the formed *combined nanoparticles could modulate* the drugs' release based on the physicochemical properties of each drug.

Unformulated daclatasvir dihydrochloride exhibited a rapid release, with approximately 100% of the drug released within 2 h. This behavior aligns with its classification as a Biopharmaceutics Classification System (BCS) Class I drug, which implies high solubility and high permeability, leading to fast dissolution and diffusion. However, when daclatasvir was encapsulated in CS-NPs, the release was significantly prolonged, extending to 24 h. This sustained release is attributed to the polymeric matrix of chitosan, which provides a diffusion barrier that slows down drug escape. Additionally, the electrostatic interactions between the positively charged chitosan and the drug molecules may further hinder diffusion, creating a controlled release effect [80].

In contrast, xanthone, a hydrophobic compound, displayed a more sustained release profile in its unformulated state, with complete release occurring over 24 h. The slower dissolution rate is primarily due to its poor water solubility, which limits its dissolution rate under physiological conditions. When xanthone was incorporated into bilosomes, the release was further sustained, with only 83% released over 72 h. This extended release is explained by the lipophilic nature of bilosomal bilayers, which facilitates the

Table 4 The optimized formula composition with the expected and the observed results

	Bilosome: CS-NPs (X_1)	PS (nm) (Y_1)	ZP (mV) (Y_2)	EE% of X (Y_3)	EE% of D (Y_4)
Expected Result	2.25: 1	231.94	−18.24	81.25	73.77
Observed Result		222.67±14.4	−19.10±3.7	83.78±3.9	78.98±2.8
*% Bias		3.99%	4.71%	3.11%	2.99%

*% Bias = (|*Expected*−*Observed*|)/*Expected* ∗ 100. Results are calculated as mean ± SD

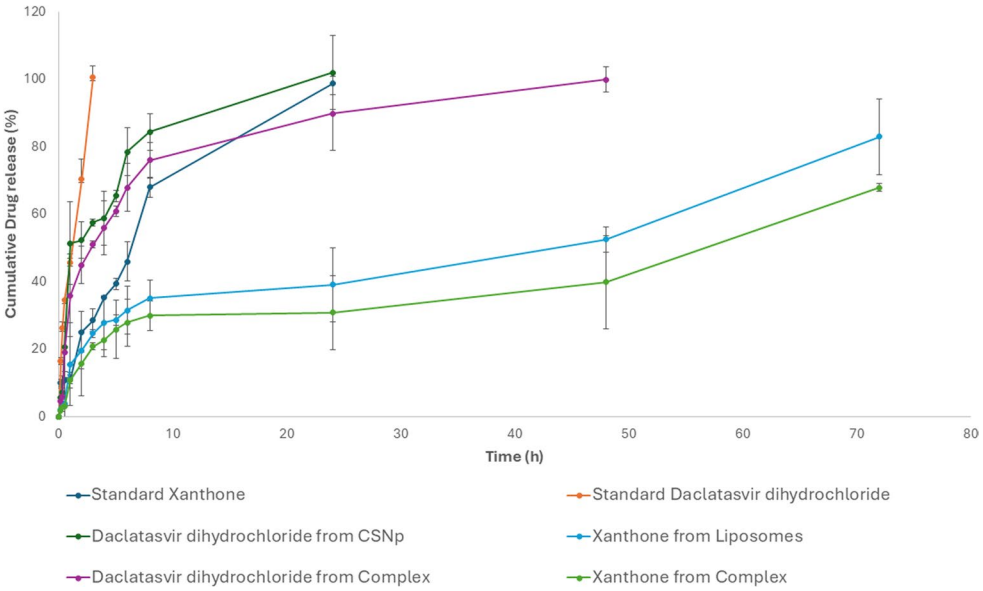

Fig. 4 *In-vitro* release rate of xanthone and daclatasvir dihydrochloride from the different formulated systems. Results are presented as mean ±SD

partitioning of hydrophobic drugs like xanthone within the lipid phase. This lipid reservoir effect slows down the drug's diffusion into the external aqueous environment. Upon further incorporation into the mixture BCNP system, the xanthone release was significantly delayed, with only about 40% released over 72 h. This marked reduction in release rate may be due to the increased diffusional resistance imposed by the presence of chitosan nanoparticles embedded within the liposomal bilayer [23]. Chitosan may interfere with or restrict drug diffusion by increasing the viscosity of the matrix, creating a denser nanoparticulate network, and potentially modifying the liposomal membrane fluidity, all of which can contribute to retarded drug release [85, 86].

The modulation in the release profile for both drugs when incorporated into the mixture nanosystem could help in Covid-19 and ARDS management as a sustained and controlled release of the anti-inflammatory or antiviral drugs in ARDS is crucial, to suppress cytokine storms (e.g., reduce IL-6, IL-1β, TNF-α), inhibit viral replication (in COVID-19-related ARDS), and control oxidative stress and neutrophilic inflammation [87]. Moreover, ARDS often requires multifaceted treatment by the co-delivery of daclatasvir and xanthone within a single formulation, which allows for synergistic action, such as viral suppression and inflammation control, which is essential in COVID-19-associated ARDS [88]. Furthermore, ARDS is associated with mucus hypersecretion and edematous barriers, which hinder drug diffusion. Chitosan enhances mucoadhesion, prolonging nanoparticle retention on pulmonary epithelium., and it also has permeation-enhancing properties, improving drug transport across inflammed and mucus-laden tissues [89].

Transmission Electron Microscopy Analysis

The surface morphology of the formed complex nanoparticles is as represented in Fig. 5. As can be observed, the particles show regular and well-defined spherical shaped vesicles. It should be mentioned that the difference in size between the electron microscope measurement and the dynamic light scattering measurement is due to measuring the hydrodynamic diameter in the dynamic light measurement, whereas the electron microscopy measures the size of the vesicles in their dry state [28]. Some particles may show a core shell structure, suggesting successful coating of the chitosan nanoparticles with the liposomal vesicles, which is common in BCNPs.

Drug Content and Polydispersity Index Measurement

The drug loading of the optimized formula was found to be 6.06% ± 0.04 for xanthone and 31.67 ± 2.45 for daclatasvir dihydrochloride. The PDI was found to be 0.302 ± 0.09, which confirms the relative homogenous size distribution of the particles within the system (< 0.4) [27].

Aerodynamic Characterization

Given that the geometrical diameter as obtained from DLS = 222.67 nm, the particle density (estimated for bilosome-chitosan nanoparticles) = 1.22 g/cm³ [33], the shape factor = 1 (spherical morphology from TEM). The AD was found to be 0.245 µm, with a GSD of 1.75, a dmm of 569 nm and a MMAD with 629 nm. This indicates an ultrafine

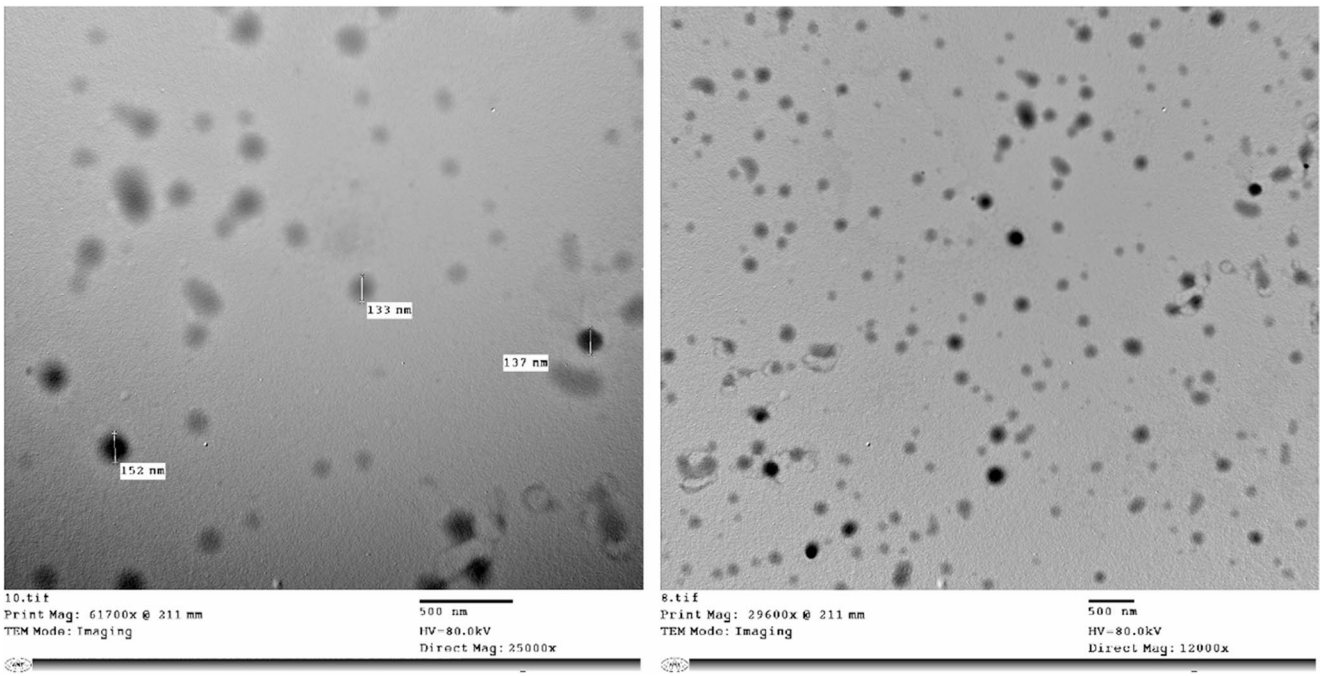

Fig. 5 TEM photographs of the optimized BCNP

aerosol with narrow size distribution, ideal for reaching the systemic drug absorption via pulmonary delivery [90]. It is worth mentioning that although MMAD is not ideal for pulmonary delivery, however the prepared formula offer some advantages as the chitosan core of the formulated system could offer a strong mucoadhesion via electrostatic binding to mucus resulting in a prolonged residence time in airways that may each to h, which also resists the mucociliary clearance [19], whereas the bile salt in bilosomes solubilizes mucus lipids and disrupts the tight junctions allowing for deeper penetration, in addition it resists phagocytosis due to its stealth effect [91].

MPPD Modeling of Lung Deposition

MMPD model was used to ensure the deposition of the nanoparticles system through the pulmonary pathway, especially that the MMAD was found to be 629 nm. The total deposited dose was found to be 36.18% in the extrathoracic region, 41.11% in the alveolar region and 22.71% in the tracheobronchial region. The high percentage value of the dose deposited in the extrathoracic region could be attributed to the nanoparticle diffusion and mucoadhesion in the nasal/oropharynx area [92]. Although the MMAD was found to be 629 nm, the pulmonary deposition in the alveolar region showed an exceptional high value which could also confirm the mucoadhesive property of the developed system. The tracheobronchial deposition is very beneficial as it could neutralize the early infection of the virus directly to bronchial viral reservoirs [12], and reduces the inflammation, by the local delivery of xanthone [5].

Thus, the MPPD results confirm that bilosome-chitosan nanoparticles (MMAD 629 nm) achieve elite pulmonary deposition (40%); defying classical aerosol physics through mucoadhesion and permeation enhancement. The regional distribution is therapeutically rational for broad-spectrum lung targeting, exploiting extrathoracic deposition for nasal-immune priming, and localized tracheobronchial delivery.

These findings, though based on theoretical and simulation models, offer scientifically robust insight into the aerodynamic behavior of the formulation and serve as an alternative when direct cascade impaction data is unavailable.

Future work may include in-vitro validation using cascade impaction or Next Generation Impactor (NGI) for further verification.

Stability Testing Analysis

The optimized formula showed excellent stability profile, as the PS, PDI, EE% of xanthone and EE% of daclatasvir dihydrochloride were not significantly (p >0.05) changed over the 6 months period either at 5 °C or at 25 °C as tabulated in Table 5. This could be due to the lyophilization and the storage of the formulation in the solid state [93]. It should be noted that the optimized formulations were obtained as lyophilized solids that can be readily reconstituted prior to administration.

Table 5 Stability study results at 2 storage temperatures

	5 °C				25 °C			
	0 month	1 month	3 month	6 month	0 month	1 month	3 month	6 month
PS (nm)	222.67 ± 14.4	224.67 ± 12.2	226.67 ± 11.5	227.67 ± 12.1	222.67 ± 14.4	226.07 ± 11.7	229.34 ± 10.4	231.71 ± 12.6
PDI	0.368 ± 0.09	0.369 ± 0.08	0.370 ± 0.07	0.371 ± 0.03	0.368 ± 0.09	0.371 ± 0.08	0.373 ± 0.06	0.375 ± 0.03
ZP (mV)	−19.1 ± 3.7	−19.4 ± 1.6	−19.7 ± 2.6	−18.90 ± 0.8	−19.1 ± 3.7	−18.8 ± 1.6	−18.7 ± 2.7	−18.4 ± 1.7
EE% of xanthone	83.78 ± 3.9	81.78 ± 2.9	81.09 ± 3.7	80.75 ± 4.6	83.78 ± 3.9	81.99 ± 7.9	79.98 ± 2.6	77.67 ± 2.2
EE% of daclatasvir dihydrochloride	73.98 ± 2.8	73.09 ± 3.1	72.67 ± 2.7	71.90 ± 3.6	73.98 ± 2.8	71.98 ± 6.9	70.52 ± 3.7	69.78 ± 5.9

*Statistically significant, using multi-way ANOVA, at $p < 0.05$. Results are presented as mean ± SD

Antiviral Activity Analysis

MTT Cytotoxicity Assay Analysis

The cytotoxicity of the optimized formula (O_1) was evaluated to demonstrate its effect on VERO-E6 cells. The results revealed that at a concentration of 1–30 µM of O_1, the cell viability was 99.3–96.9%, indicating that the optimized formula had no harmful impact and is considered safe on VERO-E6 cells. The cell viability was then decreased when the concentrations were increased up to 2 mM as shown in Fig. 6. The results showed that the 50% cytotoxic concentration (CC_{50}) value of O_1 was determined to be 19.43 µM.

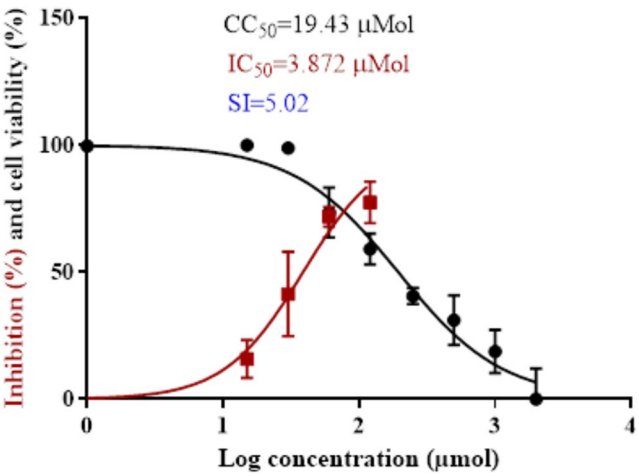

Fig. 6 Dose-response curves showing the cytotoxicity and viral inhibitory activity of O1 on Vero-E6 cells, where the cytotoxicity based on the dose–response was determined using MTT (black line), and antiviral activity of O1 using a plaque reduction assay against SARS-CoV-2 virus in Vero-E6 cells (red line). The half maximal cytotoxic concentration (CC50) and half maximal inhibitory concentrations (IC50) were calculated using nonlinear regression analysis by plotting log concentration versus normalized response (variable slope) using GraphPad Prism software (version 9.5.1). The assay was done in triplicates and the error bars represent the standard deviation. The selectivity index (SI) was calculated using the formula SI = CC50/IC50

Inhibitory Concentration 50 (IC_{50}) Determination

The antiviral activity of the optimized formula (O_1) was evaluated using a dose–response curve in a plaque reduction assay. The results indicated that the IC50 value of the optimized formula (O_1) was 3.872 µM, while the untreated infected cells exhibited virus-induced plaques, indicating significant viral replication and cytopathic effects (Fig. 5). The tested sample showed potent antiviral activity with IC_{50} = 3.872 µM against SARS-CoV-2. Consequently, the selectivity indexes (SI = CC_{50}/IC_{50}) of O_1 was calculated to be 5.02.

Dose–response data were fitted using a four-parameter logistic (4PL) nonlinear regression model in GraphPad Prism (version 9.5.1) as shown in Figure 6. The IC_{50}, defined as the concentration reducing SARS-CoV-2–induced cytopathic effect by 50% relative to untreated virus control, was 3.87 µM, while the CC_{50}, corresponding to 50% loss of cell viability, was derived from the same model. The selectivity index (SI = CC_{50}/IC_{50}) confirmed a favourable antiviral profile of the formulation.

Severe Acute Respiratory Syndrome virus (SARS CoV − 2) and Hepatitis C virus (HCV) are single-stranded positive sense RNA viruses [94]. Direct-acting antiviral agents are among the most effective treatments for HCV, offering a favorable safety profile. Since their introduction in 2011, agents such as daclatasvir dihydrochloride have been widely utilized for their reliability and efficacy [95]. Previous studies showed that the docking score may have possible eligibility of daclatasvir dihydrochloride as a potent drug against SARS-CoV-2 [96]. Daclatasvir dihydrochloride frequently inhibited the production of infectious SARS-CoV-2 in various cells such as Vero cells, with potency of 0.8 µM, targeting early events in the viral replication cycle and inhibit the induction of interleukin-6 (IL-6) and tumor necrosis factor α (TNF-α), key inflammatory mediators involved in the cytokine storm typically associated with SARS-CoV-2 infection [11].

Clinical trials have proved the efficacy of sofosbuvir and daclatasvir dihydrochloride in improving the clinical

outcome of infected patients by SARS CoV-2 and shortening the time of hospitalization among moderately infected patients, however, it does not reduce mortality rate [97, 98].

In the current study, O_1 showed relatively low SI of 5.02, which is lower than accepted range of >10 for further investigation. If the calculated SI value is between 1 and 10, re-evaluation using other biosystem(s) is advocated for confirmation [99]. In the current study, daclatasvir dihydrochloride IC_{50} in O_1 was equivalent to 3.872 µM, which is less than IC_{50} of crude daclatasvir dihydrochloride as determined by S. Bansode et al., 2023 [100] as 7 µM on Vero cells. However, in another study by C. Q. Sacramento et al., 2021 [11], the IC_{50} of daclatasvir on similar cell line was 0.8 µM. Previous studies have demonstrated that daclatasvir exhibits minimal cytotoxicity and potent antiviral activity in Vero-E6 cells. Sacramento et al. (2021) reported a CC_{50} of 31 ± 8 µM and an EC_{50} of 0.8 ± 0.3 µM, yielding a high selectivity index (SI = 39), confirming the compound's wide safety margin [11]. Similarly, xanthone-based molecules such as α- and γ-mangostins have been evaluated for antiviral effects in Vero-E6 cells, displaying CC_{50}= 5 µM and EC_{50} = 0.7–0.8 µM [101]. These findings indicate that both daclatasvir and xanthone analogues maintain cell viability at concentrations effective for viral inhibition, validating their use in antiviral formulations without confounding cytotoxic interference. Furthermore, the nanocarrier systems employed in our work, chitosan nanoparticles, and bilosomes, have been consistently reported to be biocompatible in Vero-E6 cells, where it was demonstrated that bilosomes retain cell viability across tested concentrations [102, 103]. These results collectively indicate that both carriers possess low intrinsic cytotoxicity and are suitable for drug delivery applications in antiviral studies.

It is worth mentioning that due to the strict biosafety level 3 (BSL-3) requirements and ethical contraints associated with working directly with live SARS-CoV-2 in animal models, we opted not to induce a COVID-19 infection in-vivo. Instead, we focused on an ARDS rat model, which replicates key pathological features of severe COVID-19, including pulmonary inflammation, oxidative stress, endothelial dysfunction, and alveolar damage. This approach allowed to assess the anti-inflammatory, antithrombotic, and pulmonary protective effects of the formulated daclatasvir–xanthone nanoparticles under safer and ethically feasible conditions, while still capturing the critical pathophysiological components relevant to COVID-19 complications. Furthermore, antiviral activity was assessed in-vitro using MTT assays, IC_{50} values, and selectivity index (SI) to confirm the direct efficacy against SARS-CoV-2.

In-vivo Pharmacodynamics Study

Effect on Pulmonary Levels of LncRNA-GAS5 and SP-1

As can be observed, a significant down-expression in long non-coding RNA-growth arrest specific-5 (LncRNA-GAS5) in lung tissue after the induction of ARDS using LPS ($p < 0.0001$). This result was accompanied by a significant decrease in the level of surfactant protein-1 ($p < 0.0001$). LPS is a well-known inducer compound for ARDS that causes acute lung injury by altering the pulmonary surfactants functions [104]. Recognition of LPS by a host receptor(s) leads to activation of several signal transduction cascades in lung cells activate downstream effectors, leading to the production of various inflammatory mediators. These include proinflammatory cytokines, chemokines, adhesion molecules, reactive oxygen species, and nitric oxide, produced by different cell types within the lung [105]. LncRNA-GAS5 levels were reported to be significantly downregulated in patients with ARDS. LncRNA-GAS5 is demonstrated to regulate the expression ACE2/Ang1-7 axis playing a major role in the pathogenesis of ARDS [106].

On the other hand, treatment with xanthone and daclatasvir dihydrochloride resulted in a significant up-regulation of GAS5 (at $p < 0.001$) accompanied by a significant elevation in SP-1 (at $p < 0.001$) compared to the LPS group, indicating improved pulmonary functions. Notably, the optimized xanthone–daclatasvir dihydrochloride formulation effectively restored pulmonary GAS5 and SP-1 levels ($p < 0.0001$), showing no significant difference from the normal control group, but a significant improvement compared to the free drugs' suspension-treated group at $p < 0.001$ (Fig. 7).

Effect on Pulmonary Levels of ACE-2, Angiotensin-II, Angiotensin 1–7

Results of the current study revealed a significant decrease in ACE2 activity in lung tissue after the induction of ARDS using LPS ($p < 0.001$). This result was accompanied by a significant increase in the level of angiotensin-II ($p < 0.001$) and a marked suppression of the pulmonary content of angiotensin 1–7 ($p < 0.001$). However, treatment with xanthone and daclatasvir dihydrpchloride showed a significant elevation of ACE2 activity ($p < 0.01$) and the pulmonary content of angiotensin 1–7 ($p < 0.01$) accompanied by a significant decrease in angiotensin-II ($p < 0.01$) compared to the LPS group. The improved xanthone and daclatasvir dihydrochloride formulation efficiently restored pulmonary levels of ACE2, angiotensin-II, and angiotensin 1–7 with a non-significant difference from the normal group and a noticeable significant difference from the xanthone and

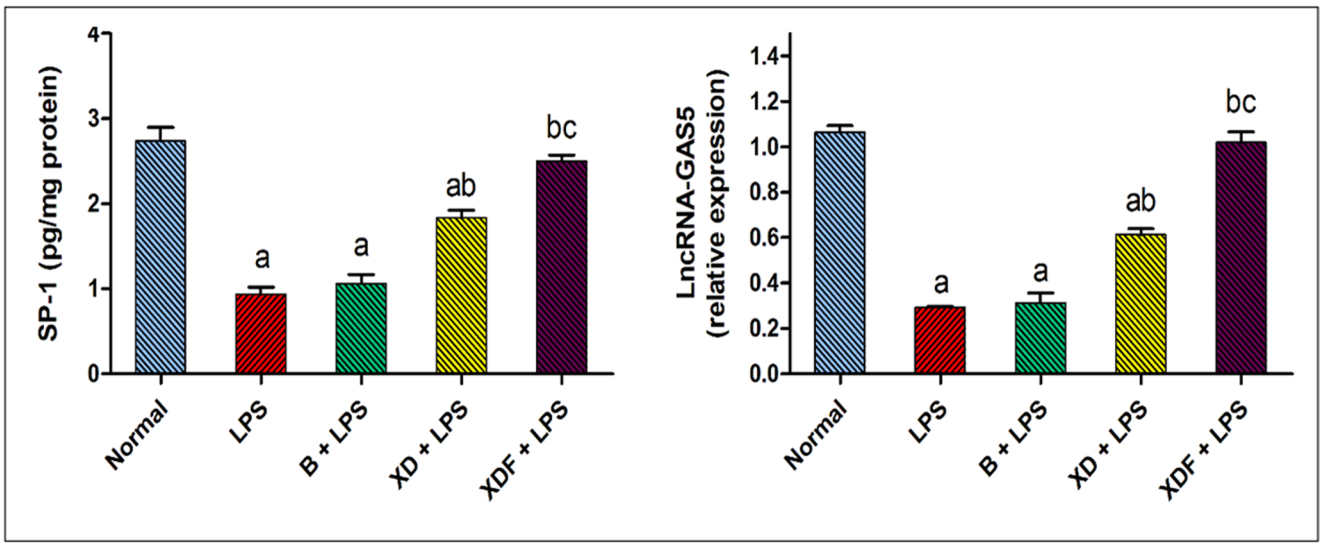

Fig. 7 Effect on pulmonary levels of SP-1 and LncRNA-GAS5 The data is presented as mean ± SEM (n = 6); where ANOVA followed by Tukey-Kramer's test was used for group comparisons, a significant difference from the normal group, b significant difference from LPS group and blank+LPS group, c:significant difference from xanthenone+ daclatasvir dihydrochloride group (at $p < 0.05$)

daclatasvir dihydrochloride suspension group ($p < 0.001$) (Fig. 8). ACE2 is demonstrated to deactivate Ang II and increase Ang 1–7 expression regulating blood pressure, body fluid balance, fibrous tissue formation, and cell proliferation [107]. More prominently, ACE2 is suggested to have a protective role in pulmonary injury through decreasing the expression levels of Ang II and increasing Ang 1–7 levels which further antagonize the actions of Ang II particularly proliferation, inflammation and vasoconstriction [41]. Furthermore, it inhibits pro-inflammatory functions by the activation of its Mas receptor [108]. Xanthone is reported to have a significant pulmonary protective effect through ACE2 activation and modulation of ACE2/Ang 1–7 pathways [41].

Effect on Pulmonary Levels of NF-kβ and TNF-α

It was observed the lungs of mice in the LPS group showed a significant increase in the proinflammatory markers NF-kβ and TNF-α compared to the control group ($p < 0.001$). In contrast, treatment with the optimized xanthone–daclatasvir dihydrochloride nanoparticle formulation resulted in a significant inhibition in pulmonary NF-kβ and TNF-α relative to LPS control at $p < 0.001$ and relative the xanthone and

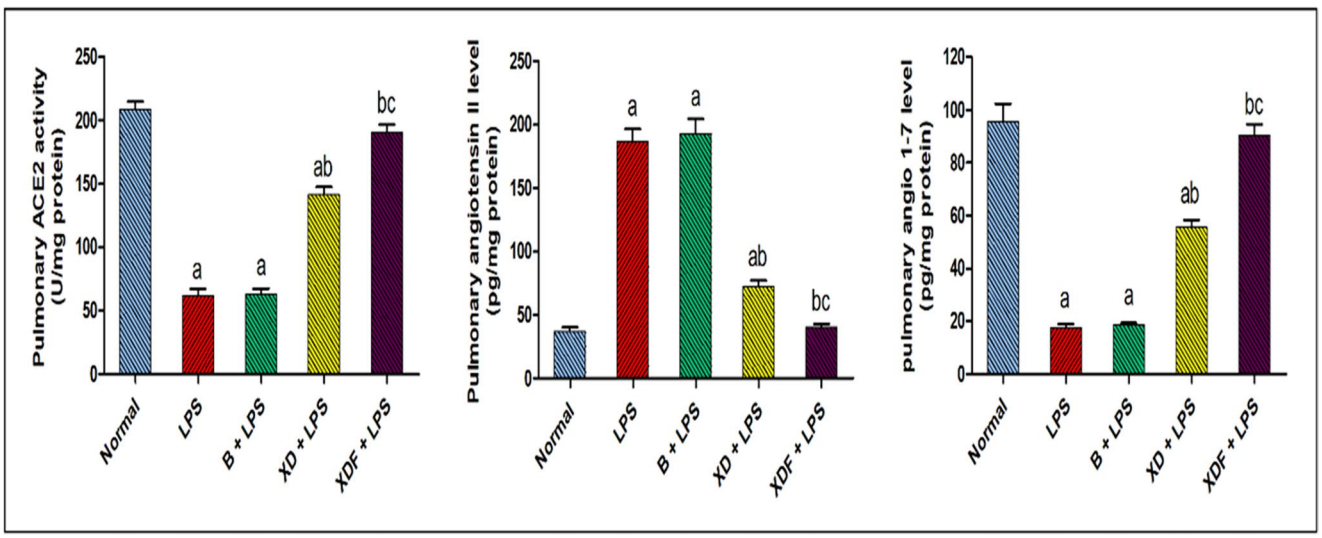

Fig. 8 Effect on pulmonary levels of ACE2, Angiotensin II and Angiotensin 1-7 The data is presented as mean ± SEM (n = 6); where ANOVA followed by Tukey-Kramer's test was used for group comparisons, a significant difference from the normal group, b significant difference from LPS group and blank+LPS group, c significant difference from xanthone+ daclatasvir dihydrochloride group (at $p < 0.05$)

daclatasvir dihydrochloride suspension groups at $p < 0.01$ (Fig. 9). These results indicate the potential role of the drugs combination when formulated to the formulated nanoparticles in suppressing NF-κB and TNF-α and their induced signaling cascades of cell death. NF-κB is a transcription factor that binds to specific DNA sequences in the nucleus, initiating the transcription and expression of inflammatory genes. Its activation can be triggered by various stimuli, including cytokines (e.g., TNF-α and IL-1β), microbial infections (such as LPS), and stress [29]. Dysregulation of NF-κB has been linked to excessive inflammation in ARDS. The NF-κB pathway promotes the production of cytokines, chemokines, and adhesion molecules, which drive inflammation, recruit immune cells, and regulate cell adhesion and differentiation. Furthermore, NF-κB activates M1 macrophages, contributing to a cytokine storm. Thus, suppressing NF-κB and TNF-α is pivotal in managing ARDS [109].

Effect on the Histological Structure of Lung Tissue

Histopathological investigation of lung tissue was used to assess the pulmonary structural damages and inflammatory cells infiltration. Lung tissue from the normal group revealed the normal structure of the bronchioles (blue arrows) with the surrounding air alveoli, orange arrows (Fig. 10a). Examination of lung tissue from the LPS group showed desquamation

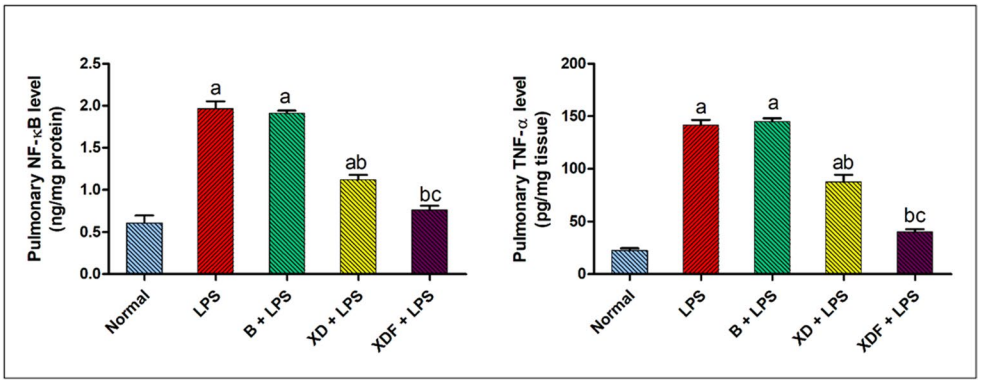

Fig. 9 Effect on pulmonary levels of NF-kβ and TNF-α The data is presented as mean ± SEM (n = 6); where ANOVA followed by Tukey-Kramer's test was used for group comparisons a significant difference from the normal group, b significant difference from LPS group and blank+LPS group, c significant difference from xanthone+ daclatasvir group (at $p < 0.05$)

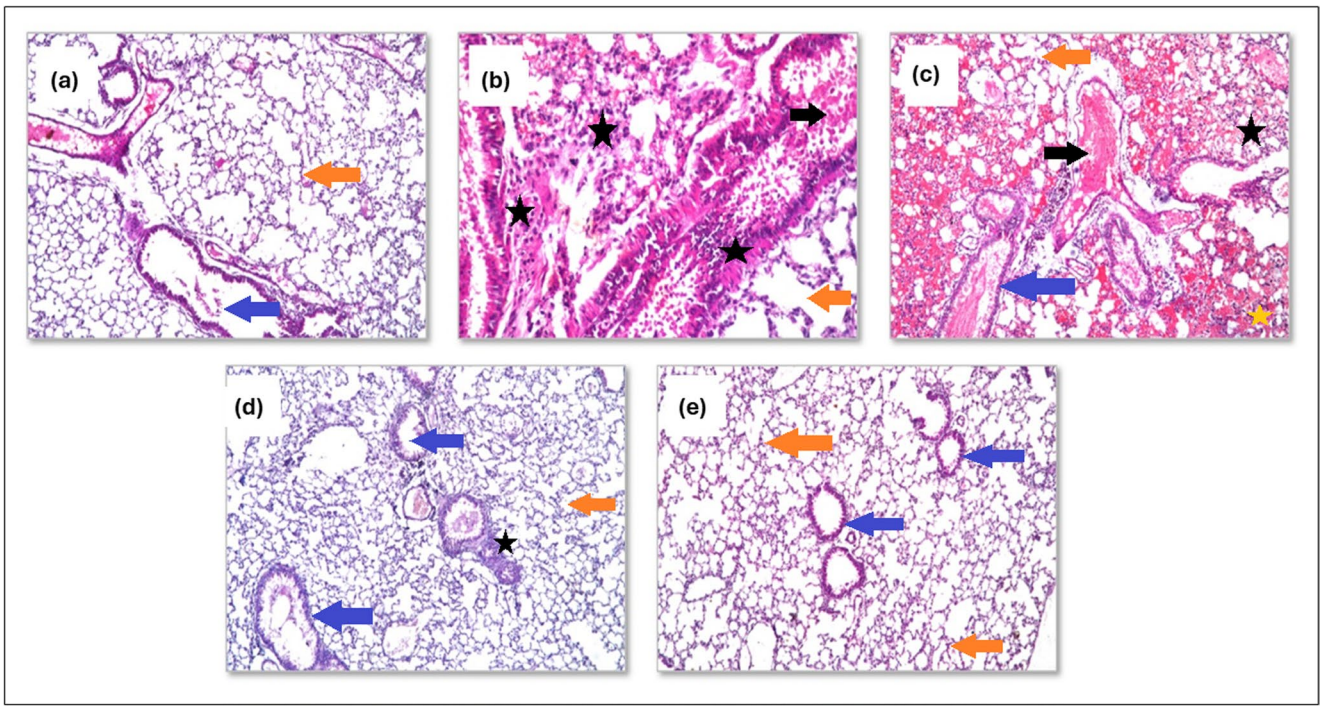

Fig. 10 Effect of xanthone and daclatasvir dihydrochloride on histological examination of the lung tissue (**a**) Normal group, (**b**) LPS group, (**c**) Blank +LPS group, (**d**) Xanthone and daclatasvir dihydrochloride +LPS, (**e**) Xanthone and daclatasvir dihydrochloride formulation (O1) + LPS group. Blue arrows lung bronchioles, orange arrows air alveoli, black arrows blood vessels congestion, and black stars inflammatory cells infiltration

of the bronchiolar lining epithelium associated with inflammatory cells infiltration (black stars) in the alveoli in between the bronchioles as well as a severe dilatation and congestion of the blood vessels in the peribronchiolar tissue (Fig. 10b). These features were also detected in the group treated with the blank formulation with focal hemorrhages and hemolyzed blood in the air alveoli associated with inflammatory cells infiltration (black stars) in the perivascular tissue (Fig. 10c). On the other hand, lung tissue from the group treated with the tested drugs suspension showed a noticeable improvement compared to the LPS group with few infiltrations of inflammatory cells in the peribronchiolar tissue (Fig. 10d). Moreover, lung tissue from the group treated with O_1 showed almost normal histological structure with no histopathological alteration (Figure 10e).

Effect on Immunohistochemical Expression Level of TNF-α

The expression of TNF-α as a major inflammatory mediator that can induce several cascades of inflammation and cell death was further assessed using immunohistochemistry assay. Lung tissue of the normal mice showed relatively negative expression of TNF-α with only few TNF-α expression surrounding the bronchioles (Fig. 11a). Lung sections from the LPS group and the group treated with the blank formulation showed strong expression of TNF-α localized in the area of inflammatory reaction and surrounding the bronchi and bronchioles (Fig. 11b and c). Lung sections from the group treated with the xanthone and daclatasivir dihydrochloride suspension showed noticeable improvement from the LPS group with mild to moderate expression of TNF-α (Figure 11d). Moreover, treatment with O_1 showed a mild expression of TNF-α around the bronchioles (Figure 11e). Comparative quantification of the immunohistochemical expression TNF-α in the lung tissue of mice from all groups is presented in (Fig. 11f).

Conclusion

In conclusion, a successful combinational drug therapy had been developed containing xanthone and daclatasvir dihydrochloride for COVID-19 treatment and control of its most common and dangerous side effects. The formulation was developed using bilosome-chitosan complex nanoparticles for the effective delivery of both drugs and to combine the advantages of those two systems. An optimized formula was prepared showing excellent stability indicating tests, where the particle was effective for the proper nanoparticle delivery with a uniform size distribution. Moreover, the zeta potential of the optimized formula was − 19 mV indicating

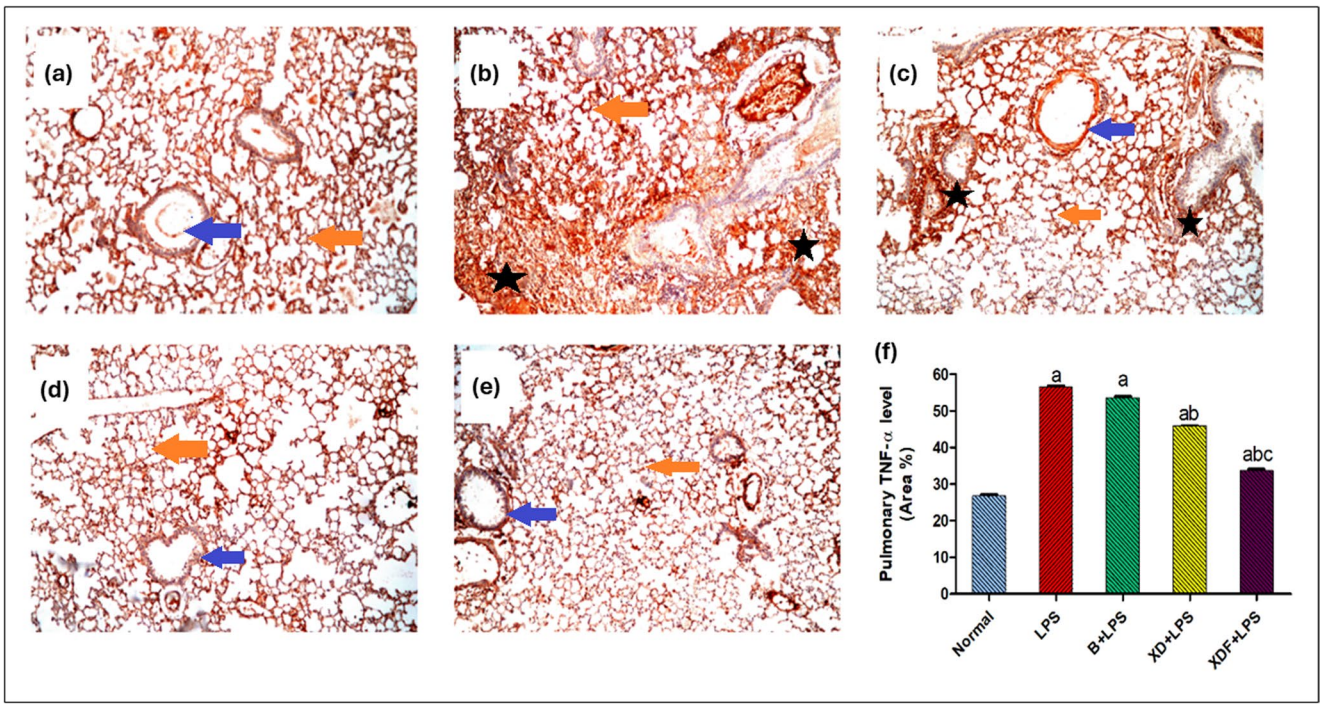

Fig. 11 Effect of xanthone and daclatasvir dihydrochloride on immunohistochemical expression level of TNF-α the lung tissue (**a**) Normal group, (**b**) LPS group, (**c**) Blank +LPS group, (**d**) Xanthone and daclatasvir dihydrochloride +LPS, (**e**) Xanthone and daclatasvir dihydrochloride formulation (O1) + LPS group, (**f**) Comparative quantification of the immunohistochemical expression TNF-α in the lung tissue of mice from all groups. Blue arrows lung bronchioles, orange arrows air alveoli, and black stars strong expression of TNF-α localized in areas of inflammatory reactions

its good stability with a suitable entrapment efficiency of each drug in its respective system. The optimized formula successfully controlled the release rate of both drugs. The formulation was assessed in-vitro using MTT assays, IC_{50} determination, and selectivity index (SI) calculations to evaluate antiviral activity and cytotoxicity. To validate its therapeutic efficacy, an ARDS rat model was established, followed by molecular (RNA expression), immunohistochemical, and histopathological analyses of lung tissue, confirming the formulation's antiviral and pulmonary protective effects. The antiviral activity of the optimized formula was assured with low SI of 5.02 and IC_{50} = 3.87 µM against SARS-CoV-2. Furthermore, its prophylactic effect against acute respiratory distress syndrome was proven through suppressing the LncRNA-GAS5/ACE2 pathway and pulmonary tissue inflammation. This study offers insights into bilosome–chitosan complexes for pulmonary delivery but has several limitations. It did not establish *in-vitro in-vivo* correlation (IVIVC) to predict clinical outcomes, and in-vivo testing was limited to small models, requiring validation in larger animals. Although the formulation shows promising physicochemical and aerosolization properties, further research is needed on long-term safety, immunogenicity, pharmacokinetics, scalability, and reproducibility, especially for industrial manufacturing. Future work will include an ex-vivo mucoadhesion assessment using porcine tracheal mucus to validate mucoadhesive performance of the optimized BCNP (O_1).

Supplementary Information The online version contains supplementary material available at https://doi.org/10.1007/s12247-025-10245-8.

Acknowledgements We deeply appreciate Dr. M. Abdelrazik, Professor of Pathology at Cairo University's Faculty of Veterinary Medicine, for his contribution in the histopathological examinations of this study. The authors would like to acknowledge Mai S. Nour from MSA University, Department of Pharmaceutical Chemistry, Faculty of Pharmacy, for her valuable assistance, insightful discussions, and guidance in the analysis of IR analysis, which significantly contributed to the completion of this research.

Author Contributions All authors contributed to the study conception and design. Material preparation, data collection, and analysis were performed by Marwa H.S. Dawoud, Mai A. Zaafan, Amr Abdelhamid, Mai A. Amer, Reham Wasfi, and Heba T.Elbalkiny. The first draft of the manuscript was written by Marwa H.S. Dawoud, Mai A. Zaafan, Amr Abdelhamid, Mai A. Amer, Reham Wasfi, and Heba T.Elbalkiny. All authors read and approved the final manuscript.

Funding Open access funding provided by The Science, Technology & Innovation Funding Authority (STDF) in cooperation with The Egyptian Knowledge Bank (EKB). This research did not receive any specific grant from funding agencies in the public, commercial, or not-for-profit sectors.

Data Availability Derived data supporting the findings of this study are available from the corresponding author on request.

Declarations

Declaration of Generative AI and AI-assisted Technologies in the Writing Process During the preparation of this work the authors used [Copilot] to improve language and readability. After using this tool, the authors reviewed and edited the content as needed and took full responsibility for the content of the publication.

Ethics statement The in-vivo study on mice was conducted in strict accordance with the ARRIVE guidelines (EU Directive 2010/63/EU for animals experiment). The study protocol was reviewed and approved by the Ethics Committee of the Faculty of Pharmacy, MSA University. All procedures involving animals were performed with the utmost care to ensure their welfare and to minimize any potential distress. (Approval number PT3/Ec3/2022PD)

Competing interests The authors declare no competing interests.

References

1. Ciotti M, Ciccozzi M, Terrinoni A, Jiang WC, Wang C Bin, Bernardini S. The COVID-19 pandemic. Crit Rev Clin Lab Sci. 2020. https://doi.org/10.1080/10408363.2020.1783198.
2. Yang L, Liu S, Liu J, Zhang Z, Wan X, Huang B, et al. COVID-19: immunopathogenesis and immunotherapeutics. Signal Transduct Target Ther. 2020. https://doi.org/10.1038/s41392-020-00243-2.
3. Huang C, Wang Y, Li X, Ren L, Zhao J, Hu Y, et al. Clinical features of patients infected with 2019 novel coronavirus in Wuhan, China. Lancet. 2020;395:497–506. https://doi.org/10.1016/S0140-6736(20)30183-5.
4. Pascarella G, Strumia A, Piliego C, Bruno F, Del Buono R, Costa F, et al. COVID-19 diagnosis and management: a comprehensive review. J Intern Med. 2020;288:192–206. https://doi.org/10.1111/joim.13091.
5. Kondo M, Zhang L, Ji H, Kou Y, Ou B. Bioavailability and antioxidant effects of a xanthone-rich mangosteen (*Garcinia mangostana*) product in humans. J Agric Food Chem. 2009;57:8788–92. https://doi.org/10.1021/jf901012f.
6. Panda SS, Chand M, Sakhuja R, Jain SC. Xanthones as potential antioxidants. Curr Med Chem. 2013;20:4481–507. https://doi.org/10.2174/09298673113209990144.
7. Jang HY, Kwon OK, Oh SR, Lee HK, Ahn KS, Chin YW. Mangosteen xanthones mitigate ovalbumin-induced airway inflammation in a mouse model of asthma. Food Chem Toxicol. 2012;50:4042–50. https://doi.org/10.1016/j.fct.2012.08.037.
8. Abdel-Fattah MM, Messiha BAS, Mansour AM. Modulation of brain ACE and ACE2 may be a promising protective strategy against cerebral ischemia/reperfusion injury: an experimental trial

in rats. Naunyn Schmiedebergs Arch Pharmacol. 2018;391:1003–20. https://doi.org/10.1007/s00210-018-1523-3.
9. Abdel-Nasser ZM, Mai A, Zaafan, Amr M, Abdelhamid. Modulation of the miR-122/Sirt-6/ACE2 axis on experimentally-induced myocardial infarction. Chem Biol Interact. 2023;36:110276.
10. Rodríguez-Puertas R. ACE2 activators for the treatment of COVID 19 patients. J Med Virol. 2020;92:1701–2. https://doi.org/10.1002/jmv.25992.
11. Sacramento CQ, Fintelman-Rodrigues N, Temerozo JR, Da Silva ADPD, Dias SDSG, Da Silva CDS, et al. In vitro antiviral activity of the anti-HCV drugs daclatasvir and sofosbuvir against SARS-CoV-2, the aetiological agent of COVID-19. J Antimicrob Chemother. 2021;76:1874–85. https://doi.org/10.1093/jac/dkab072.
12. Mattos M, Sacramento CQ, Ferreira AC, Fintelman-Rodrigues N, Pereira-Dutra FS, de Freitas CS, et al. Newly proposed dose of daclatasvir to prevent lethal SARS-CoV-2 infection in human transgenic ACE-2 mice. Viruses. 2024. https://doi.org/10.3390/v16121856.
13. Zhang T, He Y, Xu W, Ma A, Yang Y, Xu KF. Clinical trials for the treatment of coronavirus disease 2019 (COVID-19): a rapid response to urgent need. Sci China Life Sci. 2020;63:774–6. https://doi.org/10.1007/s11427-020-1660-2.
14. Suhandi C, Alfathonah SS, Hasanah AN. Potency of xanthone derivatives from *Garcinia mangostana* L. for COVID-19 treatment through angiotensin-converting enzyme 2 and main protease blockade: a computational study. Molecules. 2023. https://doi.org/10.3390/molecules28135187.
15. Nsairat H, Khater D, Sayed U, Odeh F, Al Bawab A, Alshaer W. Liposomes: structure, composition, types, and clinical applications. Heliyon. 2022. https://doi.org/10.1016/j.heliyon.2022.e09394.
16. Rudokas M, Najlah M, Alhnan MA, Elhissi A. Liposome delivery systems for inhalation: a critical review highlighting formulation issues and anticancer applications. Med Princ Pract. 2016;25:60–72. https://doi.org/10.1159/000445116.
17. Ghadi A, Mahjoub S, Tabandeh F, Talebnia F. Synthesis and optimization of Chitosan nanoparticles: potential applications in nanomedicine and biomedical engineering. Caspian J Intern Med. 2014;5:156.
18. A M, I, MA, K R, R S. Evaluation of the anti-inflammatory, antimicrobial, antioxidant, and cytotoxic effects of Chitosan Thiocolchicoside-Lauric acid nanogel. Cureus. 2023. https://doi.org/10.7759/cureus.46003.
19. Mura P, Maestrelli F, Cirri M, Mennini N. Multiple roles of chitosan in mucosal drug delivery: an updated review. Mar Drugs. 2022. https://doi.org/10.3390/md20050335.
20. Suntres ZE. Liposomal antioxidants for protection against oxidant-induced damage. J Toxicol. 2011;2011. https://doi.org/10.1155/2011/152474
21. Zacaron TM, Silva MLS, Costa MP, Silva DM, Silva AC, Apolônio ACM, et al. Advancements in chitosan-based nanoparticles for pulmonary drug delivery. Polymers. 2023. https://doi.org/10.3390/polym15183849.
22. Diebold Y, Jarrín M, Sáez V, Carvalho ELS, Orea M, Calonge M, et al. Ocular drug delivery by liposome-chitosan nanoparticle complexes (LCS-NP). Biomaterials. 2007;28:1553–64. https://doi.org/10.1016/j.biomaterials.2006.11.028.
23. Sweed NM, Zaafan MA, El-Bishbishy MH, Dawoud MHS. The pulmonary protective potential of vanillic acid-loaded TPGS-liposomes: modulation of miR-217/MAPK/NF-κb signalling pathway: vanillic acid-loaded TPGS-liposomes pulmonary protective potential. J Microencapsul. 2024;41:255–68. https://doi.org/10.1080/02652048.2024.2335166.
24. Carvalho ELS, Grenha A, Remuñán-López C, Alonso MJ, Seijo B. Mucosal delivery of Liposome-Chitosan nanoparticle complexes. Methods Enzymol. 2009;465:289–312. https://doi.org/10.1016/S0076-6879(09)65015-1.
25. Çelik Tekeli M, Yücel Ç, Ünal S, Aktaş Y. Development and characterization of insulin-loaded liposome-chitosan-nanoparticle (LCS-NP) complex and investigation of transport properties through a pancreatic beta Tc cell line. Turk J Pharm Sci. 2018;15:91–6. https://doi.org/10.4274/tjps.70783.
26. Noshi SH, Dawoud MHS, Ibrahim MS. A quality by design approach for the optimization of Olmesartan medoxomil-orodispersible lyophilisates: in vitro/in vivo evaluation. J Appl Pharm Sci. 2022;12:175–85. https://doi.org/10.7324/JAPS.2022.120617.
27. Dawoud MHS, Mannaa IS, Abdel-Daim A, Sweed NM. Integrating artificial intelligence with quality by design in the formulation of Lecithin/Chitosan nanoparticles of a poorly water-soluble drug. AAPS PharmSciTech. 2023;24:169. https://doi.org/10.1208/s12249-023-02609-5.
28. Dawoud MHS, Abdel-Daim A, Nour MS, Sweed NM. A quality by design paradigm for Albumin-Based nanoparticles: formulation optimization and enhancement of the antitumor activity. J Pharm Innov. 2023;8:1–20. https://doi.org/10.1007/s12247-022-09698-y.
29. Sweed NM, Dawoud MHS, Aborehab NM, Ezzat SM. An approach for an enhanced anticancer activity of ferulic acid-loaded polymeric micelles via MicroRNA-221 mediated activation of TP53INP1 in caco-2 cell line. Sci Rep. 2024. https://doi.org/10.1038/s41598-024-52143-y.
30. Dawoud MHS, Fayez AM, Mohamed RA, Sweed NM. Optimization of nanovesicular carriers of a poorly soluble drug using factorial design methodology and artificial neural network by applying quality by design approach. Pharm Dev Technol. 2021;26:1035–50. https://doi.org/10.1080/10837450.2021.1980009.
31. Ivey JW, Lewis D, Church T, Finlay WH, Vehring R. A correlation equation for the mass median aerodynamic diameter of the aerosol emitted by solution metered dose inhalers. Int J Pharm. 2014;465:18–24. https://doi.org/10.1016/j.ijpharm.2014.01.039.
32. Miyamoto K, Taga H, Akita T, Yamashita C. Simple method to measure the aerodynamic size distribution of porous particles generated on lyophilizate for dry powder inhalation. Pharmaceutics. 2020;12:1–14. https://doi.org/10.3390/pharmaceutics12100976.
33. Akpinar B, Fielding LA, Cunningham VJ, Ning Y, Mykhaylyk OO, Fowler PW, et al. Determining the effective density and stabilizer layer thickness of sterically stabilized nanoparticles. Macromolecules. 2016;49:5160–71. https://doi.org/10.1021/acs.macromol.6b00987.
34. Merklin JF, Taylor TW, Scrivner SM, Sorensen CM. Determination of the relative number distribution of particle sizes using photon correlation spectroscopy. Appl Opt. 1985;24:3713–7. https://doi.org/10.1364/AO.24.003713.
35. Roos RA. Aerosol technology respir. Aerosol Technology; 1999.
36. Lizonova D, Nagarkar A, Demokritou P, Kelesidis GA. Effective density of inhaled environmental and engineered nanoparticles and its impact on the lung deposition and dosimetry. Part Fibre Toxicol. 2024. https://doi.org/10.1186/s12989-024-00567-9.
37. González-González O, Ramirez IO, Ramirez BI, O'Connell P, Ballesteros MP, Torrado JJ, et al. Drug stability: ICH versus accelerated predictive stability studies. Pharmaceutics. 2022. https://doi.org/10.3390/pharmaceutics14112324.
38. Riss TL, Moravec RA, Niles AL, Duellman S, Benink HA, Worzella TJ et al. Cell Viability assays assay guidance manual. Assay Guidance Manual. 2004; pp. 1–23.
39. Amer M, Wasfi R, Ashour H, Hamed SH. Novel anti-herpes simplex activity of Chryseobacterium indologenes: genomic and metabolomic insights. Microb Pathog. 2025;204:107534.

40. Kandeil A, Mostafa A, Kutkat O, Moatasim Y, Al-karmalawy AA, Rashad AA, et al. Bioactive polyphenolic compounds showing strong antiviral activities against severe acute respiratory syndrome coronavirus 2. Pathogens. 2021. https://doi.org/10.3390/pathogens10060758.
41. Abdelhamid AM, El Deeb M, Zaafan MA. The protective effect of Xanthenone against LPS-induced COVID-19 acute respiratory distress syndrome (ARDS) by modulating the ACE2/Ang-1-7 signaling pathways. Eur Rev Med Pharmacol Sci. 2022;26(14).
42. Domscheit H, Hegeman MA, Carvalho N, Spieth PM. Molecular dynamics of lipopolysaccharide-induced lung injury in rodents. Front Physiol. 2020. https://doi.org/10.3389/fphys.2020.00036.
43. Ali M, Mohamed MI, Taher AT, Mahmoud SH, Mostafa A, Sherbiny FF, et al. New potential anti-SARS-CoV-2 and anticancer therapies of chitosan derivatives and its nanoparticles: preparation and characterization. Arab J Chem. 2023. https://doi.org/10.1016/j.arabjc.2023.104676.
44. Loutfy SA, Abdel-Salam AI, Moatasim Y, Gomaa MR, Abdel Fattah NF, Emam MH, et al. Antiviral activity of chitosan nanoparticles encapsulating silymarin (Sil-CNPs) against SARS-CoV-2 (in silico and in vitro study). RSC Adv. 2022;12:15775–86. https://doi.org/10.1039/d2ra00905f.
45. Ibrahim MA, Abdel-Aziz A, El-Sheikh A, Kamel M, Khalil A-Z, Abdelhaleem H. Hepatic effect of Sofosbuvir and Daclatasvir in thioacetamide-induced liver injury in rats. Clin Exp Hepatol. 2018;3:175–81. https://doi.org/10.5114/ceh.2018.78121.
46. Elbadawy H, Wahdan SA, El-Demerdash E. Effect of Atorvastatin on single oral pharmacokinetics and safety of Daclatasvir in rats: emphasis on P-glycoprotein and cytochrome P450. Curr Drug Metab. 2022;23:484–95. https://doi.org/10.2174/1389200223666220404134524.
47. Alhadad M, Zaafan M, El-Tanbouly DM, Elbrairy D, Zaki AIHF. Modulating the renin-angiotensin system by Eprosartan or Xanthenone drives microglial M2 polarization in a rat model of parkinson's disease via regulating the. Int Immunopharmacol. 2025;159:114950.
48. Culling C. Handbook of histopathological and histochemical techniques: including museum techniques. 2013.
49. Haque S, Whittaker M, McIntosh MP, Pouton CW, Phipps S, Kaminskas LM. A comparison of the lung clearance kinetics of solid lipid nanoparticles and liposomes by following the ^{3}H-labelled structural lipids after pulmonary delivery in rats. Eur J Pharm Biopharm. 2018;125:1–12. https://doi.org/10.1016/j.ejpb.2018.01.001.
50. Alving CR. Delivery of liposome-encapsulated drugs to macrophages. 1983;22.
51. Chang H. Clinical development of liposome-based drugs: formulation, characterization, and therapeutic efficacy. Taylor & Francis. 2012;7:49–60. https://doi.org/10.2147/IJN.S26766.
52. Franzè S, Musazzi UM, Minghetti P, Cilurzo F. Drug-in-micelles-in-liposomes (DiMiL) systems as a novel approach to prevent drug leakage from deformable liposomes. Eur J Pharm Sci. 2019. https://doi.org/10.1016/j.ejps.2019.01.013.
53. Biology BC-TJ of M. The permeability of liposomes to nonelectrolytes: I. Activation energies for permeation. J Membr Biol. 1975;20(1):205–34. https://doi.org/10.1007/BF01870637.
54. Kimelberg H. Protein-liposome interactions and their relevance to the structure and function of cell membranes. Mol Cell Biochem. 1976;10:171–90. https://doi.org/10.1007/BF01731688.
55. Carvalho ELS, Grenha A, Remuñán-López C, Alonso MJ, Seijo B. Chapter 15 mucosal delivery of liposome-chitosan nanoparticle complexes. Methods Enzymol. 2009;465:289–312. https://doi.org/10.1016/S0076-6879(09)65015-1.
56. Wang JJ, Zeng ZW, Xiao RZ, Xie T, Zhou GL, Zhan XR, et al. Recent advances of Chitosan nanoparticles as drug carriers. Taylor Francis. 2011;6:765–74. https://doi.org/10.2147/IJN.S17296.
57. Kecman S, Škrbić R, Badnjevic Cengic A, Mooranian A, Al-Salami H, Mikov M, et al. Potentials of human bile acids and their salts in pharmaceutical nano delivery and formulations adjuvants. Technol Health Care. 2020;28:325–35. https://doi.org/10.3233/THC-191845.
58. Gad S, Fetih G, Tous S, Pauletti G. Fabrication of lipid-coated chitosan nanoparticles. Br J Pharmacol. 2016;13:1–8. https://doi.org/10.9734/bjpr/2016/28714.
59. He H, Lu Y, Qi J, Zhu Q, Chen Z, Wu W. Adapting liposomes for oral drug delivery. Acta Pharm Sin B. 2019;9:36–48. https://doi.org/10.1016/j.apsb.2018.06.005.
60. Channarong S, Chaicumpa W, Sinchaipanid N, Mitrevej A. Development and evaluation of chitosan-coated liposomes for oral DNA vaccine: the improvement of peyer's patch targeting using a polyplex-loaded liposomes. AAPS PharmSciTech. 2011;12:192–200. https://doi.org/10.1208/s12249-010-9559-9.
61. Wang X, Mohammad IS, Fan L, Zhao Z, Nurunnabi M, Sallam MA, et al. Delivery strategies of amphotericin B for invasive fungal infections. Acta Pharm Sin B. 2021;11:2585–604. https://doi.org/10.1016/j.apsb.2021.04.010.
62. Beigel JH, Tomashek KM, Dodd LE, Mehta AK, Zingman BS, Kalil AC, et al. Remdesivir for the treatment of Covid-19 — final report. N Engl J Med. 2020;383:1813–26. https://doi.org/10.1056/nejmoa2007764.
63. Rahman Sabuj MZ, Islam N. Inhaled antibiotic-loaded polymeric nanoparticles for the management of lower respiratory tract infections. Nanoscale Adv. 2021;3:4005–18. https://doi.org/10.1039/d1na00205h.
64. Carvalho Silva A, Pascoal Costa M, Medeiros Zacaron T, Cristine Barbosa Ferreira K, Rodrigues Braz W, Luiz Fabri R et al. The role of inhaled Chitosan-based nanoparticles in lung cancer therapy. 2024. https://doi.org/10.3390/pharmaceutics
65. Cojocaru E, Petriș OR, Cojocaru C. Nanoparticle-based drug delivery systems in inhaled therapy: improving respiratory medicine. Pharmaceuticals. 2024. https://doi.org/10.3390/ph17081059.
66. Ahmed YM, Badawy SS, Abdel-Haleem FM. Dibenzo-18-crown-6-based carbon paste sensors for the nanomolar potentiometric determination of daclatasvir dihydrochloride: an anti-HCV drug and a potential candidate for treatment of SARS-CoV-2. Microchem J. 2022. https://doi.org/10.1016/j.microc.2022.107276.
67. Bangun H, Tandiono S, Arianto A. Preparation and evaluation of chitosan-tripolyphosphate nanoparticles suspension as an antibacterial agent. J Appl Pharm Sci. 2018;8:147–56. https://doi.org/10.7324/JAPS.2018.81217.
68. Shawky S, El-Shafai NM, El-Mehasseb IM, Shoeir KR, El-Kemary MA. Spectroscopic study of self-assembly of anti-hepatitis C virus Sofosbuvir drug with bio-polymeric nanoparticles for improving the drug release effect. Spectrochim Acta Mol Biomol Spectrosc. 2021;261. https://doi.org/10.1016/j.saa.2021.120008.
69. Alehosseini E, Shahiri Tabarestani H, Kharazmi MS, Jafari SM. Physicochemical, thermal, and morphological properties of chitosan nanoparticles produced by ionic gelation. Foods. 2022. https://doi.org/10.3390/foods11233841.
70. Oriola AO, Kar P. Naturally occurring Xanthones and their biological implications. Molecules. 2024;29. https://doi.org/10.3390/molecules29174241.
71. Severcan F, Kazanci N, Baykal, lJlkii. Siizer efik. IR and turbidity studies cholesterol-phospholipid interactions of vitamin E-membrane. 1995; 15.
72. Sun S, Liang N, Kawashima Y, Xia D, Cui F. Hydrophobic ion pairing of an insulin-sodium deoxycholate complex for oral delivery of insulin. Int J Nanomed. 2011;6:3049–56. https://doi.org/10.2147/ijn.s26450.
73. Mohsen AM, Wagdi MA, Salama A. Rutin loaded bilosomes for enhancing the oral activity and nephroprotective effects of rutin

in potassium dichromate induced acute nephrotoxicity in rats. Sci Rep. 2024. https://doi.org/10.1038/s41598-024-73567-6.
74. Parmar A, Sharma S. Derivative UV-vis absorption spectra as an invigorated spectrophotometric method for spectral resolution and quantitative analysis: theoretical aspects and analytical applications: a review. TrAC-Trends Anal Chem. 2016;77:44–53. https://doi.org/10.1016/j.trac.2015.12.004.
75. Efimova AA, Popov AS, Krivtsov GG. Anionic liposomes in contact with cationic chitosan particles. Russ J Gen Chem. 2020;90:2156–62. https://doi.org/10.1134/S1070363220110225.
76. Refai H, Hassan D, Abdelmonem R. Development and characterization of polymer-coated liposomes for vaginal delivery of sildenafil citrate. Drug Deliv. 2017;24:278–88. https://doi.org/10.1080/10717544.2016.1247925.
77. Umbrello M, Formenti P, Bolgiaghi L, Chiumello D. Current concepts of ARDS: a narrative review. Int J Mol Sci. 2017;18. https://doi.org/10.3390/ijms18010064.
78. Lee MK. Liposomes for enhanced bioavailability of water-insoluble drugs: in vivo evidence and recent approaches. Pharmaceutics. 2020. https://doi.org/10.3390/pharmaceutics12030264.
79. Jagadabi V, Nagendra Kumar PV, Mahesh K, Pamidi S, Ramaprasad LA, Nagaraju DA, Stability-Indicating. UPLC method for the determination of potential impurities and its mass by a new QDa mass detector in Daclatasvir drug used to treat hepatitis C infection. J Chromatogr Sci. 2019;57:44–53. https://doi.org/10.1093/chromsci/bmy079.
80. Herdiana Y, Wathoni N, Shamsuddin S, Muchtaridi M. Drug release study of the chitosan-based nanoparticles. Heliyon. 2022;8. https://doi.org/10.1016/j.heliyon.2021.e08674.
81. Dawoud MHS, Zaafan MA, Saleh SS, Mannaa IM, Sweed NM. Response surface optimization of a cardioprotective compound through Pharmacosomal drug delivery system: in vivo bioavailability and cardioprotective activity potential. Drug Deliv Transl Res. 2023;1–20. https://doi.org/10.1007/s13346-023-01315-w
82. Chen B, Gianolio DA, Stefano JE, Manning CM, Gregory RC, Busch MM, et al. Design, synthesis, and in vitro evaluation of multivalent drug linkers for high-drug-load antibody–drug conjugates. ChemMedChem. 2018;13:790–4. https://doi.org/10.1002/cmdc.201700722.
83. Marasini N, Skwarczynski M, Toth I. Intranasal delivery of nanoparticle-based vaccines. Ther Deliv. 2017;8:151–67. https://doi.org/10.4155/TDE-2016-0068.
84. Henning A, Schneider M, Nafee N, Muijs L, Rytting E, Wang X, et al. Influence of particle size and material properties on mucociliary clearance from the airways. J Aerosol Med Pulm Drug Deliv. 2010;23:233–41. https://doi.org/10.1089/JAMP.2009.0806.
85. Omidian H, Gill EJ, Dey Chowdhury S, Cubeddu LX. Chitosan nanoparticles for intranasal drug delivery. Pharmaceutics. 2024. https://doi.org/10.3390/pharmaceutics16060746.
86. Garg U, Chauhan S, Nagaich U, Jain N. Current advances in chitosan nanoparticles based drug delivery and targeting. Adv Pharm Bull. 2019;9:195–204. https://doi.org/10.15171/apb.2019.023.
87. Rabaan AA, Al-Ahmed SH, Muhammad J, Khan A, Sule AA, Tirupathi R, et al. Role of inflammatory cytokines in covid-19 patients: a review on molecular mechanisms, immune functions, immunopathology and immunomodulatory drugs to counter cytokine storm. Vaccines. 2021. https://doi.org/10.3390/vaccines9050436.
88. Zhou K, Qin Q, Lu J. Pathophysiological mechanisms of ARDS: a narrative review from molecular to organ-level perspectives. Respir Res. 2025. https://doi.org/10.1186/s12931-025-03137-5.
89. Ridolfi DM, Marcato PD, Justo GZ, Cordi L, Machado D, Durán N. Chitosan-solid lipid nanoparticles as carriers for topical delivery of tretinoin. Colloids Surf B Biointerfaces. 2012;93:36–40. https://doi.org/10.1016/j.colsurfb.2011.11.051.
90. Singh Kalsi H. Assessing airways deposition. physiology and pharmacokinetics of monodisperse aerosols in obstructive lung disease. 2016.
91. Chakravarthy PSA, Popli P, Challa RR, Vallamkonda B, Singh I, Swami R. Bile salts: unlocking the potential as bio-surfactant for enhanced drug absorption. J Nanopart Res. 2024. https://doi.org/10.1007/s11051-024-05985-6.
92. Vilasrao H, Pawar BPharm B. Development and characterisation of medicated wound dressings for chronic wound healing. 2013.
93. Degobert G, Aydin D. Lyophilization of nanocapsules: instability sources, formulation and process parameters. Pharmaceutics. 2021. https://doi.org/10.3390/pharmaceutics13081112.
94. Shabani M, Sadegh Ehdaei B, Fathi F, Dowran R. A mini-review on sofosbuvir and daclatasvir treatment in coronavirus disease 2019. New Microbes New Infect. 2021. https://doi.org/10.1016/j.nmni.2021.100895.
95. Geddawy A, Ibrahim YF, Elbahie NM, Ibrahim MA. Direct acting anti-hepatitis C virus drugs: clinical pharmacology and future direction. J Transl Int Med. 2017;5:8–17. https://doi.org/10.1515/jtim-2017-0007.
96. Shah B, Modi P, Sagar SR. In silico studies on therapeutic agents for COVID-19: drug repurposing approach. Life Sci. 2020. https://doi.org/10.1016/j.lfs.2020.117652.
97. Vegivinti CTR, Evanson KW, Lyons H, Akosman I, Barrett A, Hardy N, et al. Efficacy of antiviral therapies for COVID-19: a systematic review of randomized controlled trials. BMC Infect Dis. 2022. https://doi.org/10.1186/s12879-022-07068-0.
98. Chen CK, Weng TS, Chen YH, Kao JH, Chao CM. Clinical efficacy of sofosbuvir/daclatasvir in patients with COVID-19: a systematic review and meta-analysis of randomized trials. Expert Rev Clin Pharmacol. 2022. https://doi.org/10.1080/17512433.2022.2103539.
99. Indrayanto G, Putra GS, Suhud F. Validation of in-vitro bioassay methods: application in herbal drug research. Profiles Drug Subst Excip Relat Methodol. 2021;46:273–307. https://doi.org/10.1016/bs.podrm.2020.07.005.
100. Bansode S, Singh PK, Tellis M, Chugh A, Deshmukh N, Gupta M, et al. A comprehensive molecular and clinical investigation of approved anti-HCV drugs repurposing against SARS-CoV-2 infection: a glaring gap between benchside and bedside medicine. Vaccines. 2023. https://doi.org/10.3390/vaccines11030515.
101. Suroengrit A, Cao V, Wilasluck P, Deetanya P, Wangkanont K, Hengphasatporn K, et al. Alpha and gamma mangostins inhibit wild-type B SARS-CoV-2 more effectively than the SARS-CoV-2 variants and the major target is unlikely the 3C-like protease. Heliyon. 2024. https://doi.org/10.1016/j.heliyon.2024.e31987.
102. Frigaard J, Jensen JL, Galtung HK, Hiorth M. The potential of chitosan in nanomedicine: an overview of the cytotoxicity of chitosan based nanoparticles. Front Pharmacol. 2022. https://doi.org/10.3389/fphar.2022.880377.
103. Zakaria MY, Abd El-Halim SM, Beshay BY, Zaki I, Abourehab MAS. Poly phenolic phytoceutical loaded nano-bilosomes for enhanced caco-2 cell permeability and SARS-CoV 2 antiviral activity': in-vitro and insilico studies. Drug Deliv. 2023. https://doi.org/10.1080/10717544.2022.2162157.
104. Rittirsch D, Flierl MA, Day DE, Nadeau BA, Mcguire SR, Hoesel LM et al. Acute lung injury induced by lipopolysaccharide is independent of complement activation . Am J Immunol. 2008;180.
105. Fiala A, Slagle C, Legband N, Aghabaglou F, Buesing K, Borden M, et al. Treatment of a rat model of LPS-induced ARDS via peritoneal perfusion of oxygen microbubbles. J Surg Res. 2019;246:450–6.
106. Ayeldeen G, Shaker OG, Amer E, Zaafan MA, Herzalla MR, Keshk MA, et al. The impact of lncRNA-GAS5/miRNA-200/

ACE2 molecular pathway on the severity of COVID-19. Curr Med Chem. 2023;31:1142–51. https://doi.org/10.2174/0929867330666230515144133.
107. Abdel-Fattah MM, Elgendy ANAM, Mohamed WR. Xanthenone, ACE2 activator, counteracted gentamicin-induced nephrotoxicity in rats: impact on oxidative stress and ACE2/Ang-(1–7) signaling. Life Sci. 2021. https://doi.org/10.1016/j.lfs.2021.119387.
108. Simões E Silva AC, Silveira KD, Ferreira AJ, Teixeira MM. ACE2, angiotensin-(1–7) and Mas receptor axis in inflammation and fibrosis. Br J Pharmacol. 2013;169:477–92. https://doi.org/10.1111/bph.12159.
109. Huang Q, Le Y, Li S, Bian Y. Signaling pathways and potential therapeutic targets in acute respiratory distress syndrome (ARDS). Respir Res. 2024. https://doi.org/10.1186/s12931-024-02678-5.